

1 **Transported African Dust in the Lower Marine Atmospheric Boundary Layer is Internally
2 Mixed with Sea Salt Contributing to Increased Hygroscopicity and a Lower Lidar
3 Depolarization Ratio**

4 Sujan Shrestha¹, Robert E. Holz^{2*}, Willem J. Marais², Zachary Buckholtz², Ilya Razenkov²,
5 Edwin Eloranta², Jeffrey S. Reid³, Hope E. Elliott^{1,a}, Nurun Nahar Lata⁴, Zhen Cheng⁴, Swarup
6 China⁴, Edmund Blades¹, Albert D. Ortiz¹, Rebecca Chewitt-Lucas⁵, Alyson Allen¹, Devon
7 Blades¹, Ria Agrawal¹, Elizabeth A. Reid³, Jesus Ruiz-Plancarte⁶, Anthony Bucholtz⁶, Ryan
8 Yamaguchi⁶, Qing Wang⁶, Thomas Eck⁷, Elena Lind⁷, Mira L. Pöhlker⁸, Andrew P. Ault⁹,
9 Cassandra J. Gaston^{1*}

10 ¹Department of Atmospheric Sciences, Rosenstiel School of Marine, Atmospheric, and Earth
11 Science, University of Miami, FL, USA

12 ²Space Science and Engineering Center (SSEC), University of Wisconsin-Madison, WI, USA

13 ³U.S. Naval Research Laboratory, Monterey, CA, USA

14 ⁴Environmental Molecular Sciences Laboratory, Pacific Northwest National Laboratory,
15 Richland, WA, USA

16 ⁵Caribbean Institute for Meteorology and Hydrology, Barbados

17 ⁶Department of Meteorology, Naval Postgraduate School, Monterey, CA, USA

18 ⁷NASA Goddard Space Flight Center, Greenbelt, MD, USA

19 ⁸Atmospheric Microphysics Department, Leibniz Institute for Tropospheric Research, Leipzig,
20 Germany

21 ⁹Department of Chemistry, University of Michigan, MI, USA

22 ^anow at Department of Biological & Environmental Sciences, Wittenberg University, Springfield,
23 OH, USA

24 *Corresponding Author: Cassandra J. Gaston: Email: cgaston@miami.edu, Phone: (305)-421-
25 4979 and Robert E. Holz: Email: reholz@ssec.wisc.edu

26 **Abstract**

27 Saharan dust is frequently transported across the Atlantic, yet the chemical, physical, and
28 morphological transformations dust undergoes within the marine atmospheric boundary layer
29 (MABL) remain poorly understood. These transformations are critical for understanding dust's
30 radiative and geochemical impacts, its representation in atmospheric models, and detection via
31 remote sensing. Here, we present coordinated observations from the Office of Naval Research's
32 Moisture and Aerosol Gradients/Physics of Inversion Evolution (MAGPIE) August 2023
33 campaign at Ragged Point, Barbados. These include vertically resolved single-particle analyses,
34 mass concentrations of dust and sea spray, and High Spectral Resolution Lidar (HSRL)
35 retrievals. Single-particle data show that dust within the Saharan Air Layer (SAL) remains
36 externally mixed, with a corresponding high HSRL-derived linear depolarization ratio (LDR) at
37 532 nm of ~0.3. However, at lower altitudes, dust becomes internally mixed with sea spray, and
38 under the high humidity (>80%) of the MABL undergoes hygroscopic growth, yielding more
39 spherical particles, suppressing the LDR to <0.1; even in the presence of high dust loadings (e.g.,
40 ~120 $\mu\text{g}/\text{m}^3$). This low depolarization in the MABL is likely due to a combination of the
41 differences between the single scattering properties of dust and spherical particles, and the
42 potential modification of the dust optical properties from an increased hygroscopicity of dust
43 caused by the mixing with sea salt in the humid MABL. These results highlight the importance
44 of the aerosol particle mixing state when interpreting LDR-derived dust retrievals and estimating
45 surface dust concentrations in satellite products and atmospheric models.

46 **1. Introduction**

47 The transport of Saharan dust across the North Atlantic Basin throughout the year is one
48 of the largest aerosol phenomena observable from space. The most intensive events often occur
49 during the boreal summer when large quantities of dust are lofted and advected westward by
50 trade winds within the Saharan Air Layer (SAL), a well-defined elevated layer extending from
51 ~2 to 5 km above mean sea level (AMSL) (e.g., Carlson and Prospero, 1972; Karyampudi et al.,
52 1999; Adams et al., 2012; Tsamalis et al., 2013; Mehra et al., 2023). This conceptual model of
53 African dust transport is frequently reinforced by satellite and ground-based remote sensing,
54 particularly lidar (Burton et al., 2012, 2015), multi-angle imager (Kalashnikova et al., 2013),
55 polarimetric (Huang et al., 2015) or combination of these observations (Moustaka et al., 2025)
56 that rely on dust's asphericity to differentiate coarse mode dust from other aerosol sources such
57 as hydrated sea spray. These techniques often detect little dust within the lower marine
58 atmospheric boundary layer (MABL). However, it is well known that exceptionally high dust
59 concentrations are often directly measured in the MABL (e.g., Reid et al., 2003b; Zuidema et al.,
60 2019; Elliott et al., 2024; Mayol-Bracero et al., 2025) and these layers are regularly forecast by
61 operational dust transport models (Xian et al., 2019). This contradiction between the common
62 conceptual model fueled by remote sensing of elevated dust layers versus evidence of significant
63 near-surface dust mass concentrations by in situ observations raises a critical question, is there an
64 observational gap in the detection and characterization of dust within the MABL?

65 Among the methods to speciate airborne dust from other aerosol particle types, the most
66 common benchmark is to rely on dust's asphericity, and its impact on lidar's linear depolarization
67 ratio (LDR). The LDR is based on a lidar's range-resolved measurement of the fraction of
68 backscattered light by aerosol particles that become depolarized from the original polarized laser

69 pulse. Backscattered light from homogeneous spherical particles, such as hydrated sea salt, has
70 low depolarization (e.g., LDR remains minimal) whereas particles with asymmetry such as dry,
71 irregular dust will return a partially depolarized signal, typically \sim 0.25-0.40 (Murayama et al.,
72 1999; Ansmann et al., 2012; Burton et al., 2012; Freudenthaler et al., 2009; Sakai et al., 2010;
73 Groß et al., 2016).

74 The assertion that dust can be isolated from other aerosol types such as in the references
75 above is well supported by both theoretical foundations and numerous observations of elevated
76 dust plumes. An important assumption in the detection of dust via the LDR is that the dust is not
77 hygroscopic. In situ observations of dust hygroscopicity in the MABL, typically using the
78 standard technique of drying and subsequently rehydrating particles ahead of nephelometer
79 measurements (Orozco et al., 2016), have suggested MABL dust is not significantly hygroscopic
80 (Li-Jones et al., 1998; Zhang et al., 2014). Thus, it is often assumed that dust in the humid
81 MABL will retain its aspherical shape and remain tracible via the LDR. However, even freshly
82 emitted dust or that which is sampled well within a dust plume can contain soluble minerals that
83 should be inherently hygroscopic and could affect detection of dust via the LDR (Koehler et al.,
84 2007; Reid et al., 2003a).

85 Contradictory observations have introduced uncertainty in the interpretation of lidar
86 observations for dust detection in the MABL. For example, during the SALTRACE campaign in
87 Barbados, lidar-derived LDR measurements within the lower MABL were 0.15 ± 0.02 ,
88 suggesting approximately equal parts spherical and non-spherical particles, despite in-situ
89 observations indicating surface dust mass concentrations as high as $40 \mu\text{g}/\text{m}^3$ (Groß et al., 2016;
90 Weinzierl et al., 2017). Groß et al. (2016) also reported that dust mass concentrations exceeding
91 $40 \mu\text{g}/\text{m}^3$ could be underestimated by up to 50% by lidar-derived depolarization measurements,

92 in part due to the dominant influence of sea spray in the MABL that introduces large
93 concentrations of hydrated, spherical particles that reduce the overall depolarization signal.
94 Tsamalis et al. (2013) emphasized that the polluted dust aerosol type is often misclassified or
95 detected less often in spaceborne CALIOP observations due to low depolarization signals
96 resulting from dust mixing with other aerosol types such as biomass burning, marine or
97 anthropogenic aerosols (Yang et al., 2022; Kong et al., 2022). The relationship between dust
98 mass and depolarization has important implications for how the depolarization ratio is used to
99 infer surface-level dust concentrations in air quality forecasts and climate models. Since satellite
100 retrievals and column-integrated techniques lack vertical resolution, they may fail to capture
101 such near-surface morphological changes in dust (Li et al., 2020). If depolarization-based
102 methods underestimate dust presence near the surface under marine conditions, it could
103 introduce systematic errors in dust-related radiative forcing and deposition estimates. A similar
104 concern exists for multi-angle imagers and polarimetric retrievals that depend on assumptions of
105 particle asymmetry to detect and quantify dust.

106 During August 2023, the Office of Naval Research (ONR) initiated the Moisture and
107 Aerosol Gradients/Physics of Inversion Evolution (MAGPIE) field campaign at the University of
108 Miami's Barbados Atmospheric Chemistry Observatory (BACO) at Ragged Point, Barbados to
109 map the inhomogeneity of the MABL. Central to MAGPIE are studies to identify information
110 lost when one conceptualizes the MABL as a series of uniform layers (e.g., surface layer, mixed
111 layer, entrainment or detrainment zones, etc.). While MAGPIE's core objectives focus on
112 atmospheric flows and fluxes with an emphasis on active remote sensing, aerosol particles and
113 their optical closure were implicitly a core mission element because light scattering by these
114 particles can be used to track atmospheric motion. MAGPIE collaborated across U.S. federal

115 agencies, academic institutions, and the Caribbean Institute for Meteorology and Hydrology
116 (CIMH) and included observations from ground-based aerosol particle samplers and instruments
117 at BACO along with local flights from the Naval Postgraduate School (NPS) CIRPAS Twin Otter
118 (CTO) aircraft. Central to the mission was the University of Wisconsin Space Sciences and
119 Engineering Center's (SSEC) High Spectral Resolution Lidar (HSRL; Eloranta et al., 2008).
120 Here, single particle and bulk analyses are used to evaluate how measured dust and sea salt mass
121 concentrations relate to HSRL-derived particulate LDR. In Section 2, we provide a brief
122 overview of measurements, and in Section 3.1 a timeseries analysis of particle and lidar data,
123 demonstrating nonlinearity between dust and sea salt mass ratios to lidar LDR. In Sections 3.2
124 and 3.3, we provide vertically resolved single particle data from the CTO aircraft and ground-
125 based samples, respectively, to help explain the anomalies. In Section 4, we provide a discussion
126 and study conclusions.

127 **2. Methods and materials**

128 **2.1. Sampling Site and Campaign Overview**

129 Ground-based aerosol particle and lidar measurements were conducted at the BACO site
130 on Ragged Point (13°6'N, 59°37'W) for August 2023. Situated at the easternmost point of the
131 Caribbean, BACO offers an optimal location for intercepting long-range transported Saharan
132 dust with minimal interference from local, anthropogenic emissions due to the prevalent Easterly
133 trade winds (Prospero et al., 2021; Gaston et al., 2024; Zuidema et al., 2019). Continuous aerosol
134 particle measurements have been conducted there for over 50 years, providing a unique long-
135 term observational record. The site is equipped with a tower that is 17 m high and is placed atop
136 a 30 m high bluff giving an altitude of ~50 m above sea level. While the measurements are not
137 taken directly at ground level, they are representative of the near surface MABL and are

138 routinely referred to as surface observations in prior Barbados studies (e.g., Zuidema et al.,
139 2019).

140 MAGPIE leveraged multi-platform measurements including aerosol particles collected at
141 the top of the BACO sampling tower and aboard the CTO aircraft to investigate vertical
142 gradients in aerosol particle chemical and morphological properties. For the 2023 campaign, the
143 focus is centered around the largest dust events of the year observed between August 11-18,
144 2023. A total of five research flights were conducted during this period, with two samples
145 collected per flight, resulting in ten samples covering a range of altitudes from 30 m to 3 km
146 AMSL.

147 **2.2. Dust Mass Concentration Measurement**

148 Aerosol particles were collected on top of the BACO tower using high-volume samplers
149 with Total Suspended Particulate (TSP) inlets and fitted with cellulose filters (Whatman-41, 20
150 μm pore size) with a particle size cutoff at 80-100 μm in diameter due to the geometry of the
151 rainhat as described in Royer et al. (2023). Procedural filter blanks were collected every five
152 days and processed alongside the daily filter samples. A quarter of each filter was sequentially
153 extracted three times using a total of 20 mL of Milli-Q water to remove soluble components.
154 Following extraction, the filters were combusted at 500 $^{\circ}\text{C}$ overnight in a muffle furnace. The
155 residual ash mass was weighed and corrected for background contributions by subtracting the
156 ash mass obtained from the procedural blank. The net ash mass was multiplied by a correction
157 factor of 1.3 to account for the loss of any soluble or volatile components during the extraction
158 and combustion process (Prospero, 1999; Zuidema et al., 2019). While some soluble components
159 such as halite may be lost during the extraction process, the applied correction factor of 1.3 is
160 intended to conservatively account for these potential losses, supporting more robust dust mass

161 estimates. Moreover, halite is not a major constituent of Saharan dust, as previous studies report
162 its contribution rarely exceeds 3% by weight (Scheuvens et al., 2013), making any bias from its
163 loss during the extraction process unlikely to be significant.

164 **2.3. Sea Salt Concentration Measurement**

165 The filtrate collected after dust extraction on the daily filter samples and procedural
166 blanks was then analyzed using ion chromatography (IC; Dionex Integrion HPIC System;
167 Thermo Scientific). The samples were analyzed in triplicate for cations and anions and corrected
168 for procedural blanks. Details of our IC analysis procedure can be found in Royer et al. (2025).
169 Sodium (Na^+) is commonly used as a conservative tracer for sea spray particles, therefore, the
170 Na^+ concentrations measured by IC analysis were converted to equivalent sea salt concentrations
171 by applying a multiplication factor of 3.252 (Eqn. 1) (Gaston et al, 2024; Prospero, 1979).

172
$$\text{Sea salt concentration} = [\text{Na}^+] * 3.252 \quad \text{Eqn. 1}$$

173 **2.4. In-situ Ground-based Aerosol Optical Measurement**

174 BACO is part of NASA's AErosol RObotic NETwork (AERONET). We used AERONET
175 level 2 aerosol optical depth (AOD at 500 nm) and fine mode AOD (at 500 nm) from the
176 AERONET spectral deconvolution retrieval (O'Neill et al., 2003) to identify the times of dust
177 intrusion during the sampling campaign (Giles et al., 2019; Holben et al., 1998).

178 **2.5. Single-Particle Analysis and Mixing State**

179 Aerosol particle mixing state describes how chemical species are distributed across the
180 particle population (Winkler, 1973; Riemer et al., 2019). Single-particle analysis offers a
181 powerful approach for analyzing this complexity, providing direct insight into the internal
182 composition and variability of individual particles (Reid et al., 2003a; Ault et al., 2014, 2012;

183 Royer et al., 2023; Casuccio et al., 1983; Kim et al., 1987; Andreae et al., 1986; Zhang et al.,
184 2003; Levin et al., 2005; Kandler et al., 2018). We used computer-controlled scanning electron
185 microscopy (SEM, Quanta from Thermo Fisher Scientific, equipped with a FEI Quanta digital
186 field emission gun at 20 kV and 480 pA electron current) coupled with energy-dispersive X-ray
187 spectroscopy (EDX, Oxford UltimMax100) (CCSEM/EDX) at the Environmental Molecular
188 Sciences Laboratory (EMSL) located at the Pacific Northwest National Laboratory (PNNL) to
189 characterize single particles. EDX spectra are collected for semi-quantitative analysis of the
190 particle elemental composition, and our analysis focused on 16 elements commonly found in
191 atmospheric aerosol particles: carbon (C), nitrogen (N), oxygen (O), sodium (Na), magnesium
192 (Mg), aluminum (Al), silicon (Si), phosphorous (P), sulfur (S), chlorine (Cl), potassium (K),
193 calcium (Ca), vanadium (V), manganese (Mn), iron (Fe), and nickel (Ni). This analysis was
194 conducted for particles collected on the BACO tower and aboard the CTO aircraft.

195 **2.5.1. Ground-based Particulate Samples for Single Particle Analysis**

196 Ambient aerosol particles were sampled on top of BACO's 17 m tower using a three-stage
197 cascade impactor (Microanalysis Particle Sampler, MPS-3; California Measurements, Inc.), that
198 separates particles into aerodynamic diameter ranges of 2.5-5.0 μm (stage 1), 0.7-2.5 μm (stage
199 2), and 0.05-0.7 μm (stage 3). Samples were collected for 30 minutes at 2 L/min each day.
200 Particles were deposited onto carbon-coated copper grids (Ted Pella, Inc.) and analyzed using
201 CCSEM/EDX. No conductive coating (e.g., gold or carbon) was applied to the samples collected
202 on the ground as the conductivity of the copper grid bars minimized possible impacts from
203 charging effects. However, Cu signals from CCSEM/EDX were excluded due to interference
204 from the substrate. In contrast, C films are thin and highly transparent to electrons. Although C
205 signals are present in all spectra due to the support film, the C layer is fine-grained and

206 minimally interferes with particle morphology. Moreover, C together with O, serves as a useful
207 qualitative indicator for identifying organic particles, defined by a combined C + O contribution
208 exceeding 95 %. In this study, N was not used for quantification, nor did we label it in the EDX
209 spectra of particles. Elemental signals were considered valid for further analysis only when
210 exceeding a 2% threshold composition detected by EDX spectra. Over 1,000 individual particles
211 were analyzed per sample. Post-processing of CCSEM/EDX data was conducted using a k-
212 means clustering algorithm (Ault et al., 2012; Shen et al., 2016; Royer et al., 2023) to group
213 particles by similarity in composition and morphology. Clusters were classified into particle
214 types primarily based on semiquantitative elemental composition obtained from EDX analysis,
215 supported by particle size, morphology, and comparison with prior studies. Mineral dust particles
216 were identified by the presence of aluminosilicate elements (Si, Al, and Fe) characteristic of
217 crustal minerals (Hand et al., 2010; Krueger et al., 2004; Levin et al., 2005; Krejci et al., 2005;
218 Denjean et al., 2015). Fe was detected in ~80 % of mineral dust particles at relative area
219 abundances of 10-15 %. Sea spray particles were characterized by strong Na and Cl peaks,
220 indicative of halite (NaCl) and confirming their marine origin (Bondy et al., 2018). Aged sea
221 spray particles were identified by Cl depletion accompanied by enrichment in S, consistent with
222 heterogeneous reactions that replace Cl with sulfate or nitrate (Ault et al., 2014; Royer et al.,
223 2023, 2025). Mineral dust particles were observed to be both internally mixed with sea spray and
224 externally mixed (Royer et al., 2023, 2025; Kandler et al., 2018; Harrison et al., 2022; Aryasree
225 et al., 2024). These internally mixed dust and sea spray particles exhibited heterogeneous
226 compositions containing both dust-derived (Si, Al, Fe, Mg) and marine-derived (Na, Cl, Mg)
227 components, with Mg potentially originating from both sources. Organic particles were
228 dominated by C and O (>95 %), with minor inorganic elements, and typically appeared as

229 spherical or gel-like structures. Some displayed Mg-rich shells with sea salt cores, consistent
230 with primary marine organics formed via bubble-bursting at the ocean surface (Ault et al., 2013;
231 Gaston et al., 2011; Chin et al., 1998). Sulfate-rich particles exhibited strong sulfur peaks with
232 accompanying C and O signals, indicative of marine secondary aerosols (e.g., ammonium sulfate
233 or bisulfate) and frequently contained an organic fraction (O'Dowd and de Leeuw, 2007; Royer
234 et al., 2023).

235 **2.5.2. Airborne Particulate Samples for Single Particle Analysis**

236 Aerosol samples were also collected onboard the CTO using an isokinetic inlet and deposited
237 onto isopore membrane filters (47 mm filter, 0.8 μm pore size). An overview of the airborne
238 sampling technique can be found in the Supporting Information (SI Text S1). The CTO's primary
239 inlet has an intrinsic 50 % cutpoint of $\sim 3.5 \mu\text{m}$ in aerodynamic diameter. Due to limitations
240 associated with Teflon filter material, automated computer-controlled SEM was not feasible, and
241 these airborne samples were analyzed manually using SEM/EDX. To prevent particle charging
242 during imaging, filters were sputtered with a gold-coating of 10 nm thickness prior to analysis. A
243 total of 40, 21, and 52 particles from 250 nm to 25 μm diameter were manually analyzed from
244 samples collected within the SAL, above, and below cloud base heights (CBH), respectively,
245 providing a primarily qualitative assessment. The CBH was identified for each flight as the first
246 maximum in profile relative humidity, typically near saturation. Details of airborne sample
247 collection date and times, durations, altitudes, and corresponding CBH are provided in Table S1.
248 Particles were selected randomly across the filter area without targeting specific particle types or
249 sizes to reduce selection bias. All filter handling was performed in a laminar flow hood, and
250 filters were stored individually in sealed Teflon-taped Petri dishes to avoid any contamination.
251 The number of particles analyzed is reported in Table S2 of the SI. To quantify statistical

252 uncertainty, we calculated 95% confidence intervals for the number fraction of each particle class
253 assuming binomial sampling. The major particle types show varying levels of statistical
254 precision. For example, mineral dust is clearly dominant in the SAL ($90 \pm 9\%$) and statistically
255 distinct from mixed dust and sea spray particles, whereas above cloud top and below cloud base,
256 mineral dust and internally mixed dust and sea spray fractions have overlapping confidence
257 intervals, indicating comparable abundance within uncertainty. Thus, while the data robustly
258 supports dust dominance in the SAL, compositional differences among dust and dust mixed with
259 sea spray particle types in the above cloud top and below cloud base should be interpreted
260 qualitatively. Whenever possible, ground-based measurements were coordinated to coincide with
261 periods when the CTO aircraft intercepted the BACO location or its vicinity. Single particle
262 analysis from aircraft sampling, presented in Section 3.2, serves as a comparative reference to
263 the more comprehensive in-situ ground-based dataset, which includes $\sim 24,000$ analyzed
264 particles. The sulfate and organic particle types were absent in the airborne samples. This is
265 likely due, in part, to the use of isopore filters with a relatively large pore size (0.8 μm), that may
266 have limited the collection efficiency of finer sulfate and organic rich particles.

267 **2.6. High Spectral Resolution Lidar (HSRL)**

268 The SSEC HSRL was deployed during the summer 2023 MAGPIE campaign to
269 characterize the vertical distribution of aerosol particle scattering properties over Ragged Point.
270 The HSRL system used in this study can provide range-resolved profiles of particulate
271 backscatter and depolarization at high spatial and temporal resolution. Details on the SSEC
272 HSRL can be found elsewhere (Razenkov, 2010; Eloranta et al., 2008; Reid et al., 2025). Briefly,
273 the SSEC HSRL operates at a wavelength of 532 nm and separates molecular and particulate
274 backscatter signals using a narrowband iodine absorption filter. This configuration enables

275 accurate, independent retrievals of particulate backscatter ($\text{m}^{-1} \text{ sr}^{-1}$) within close proximity to the
276 ocean surface, as well as calibrated extinction (m^{-1}) and extinction-to-backscatter ratio (i.e., the
277 lidar ratio) measurements. The HSRL also contains an elastic backscatter channel of 1064 nm.
278 Long term Raman lidar measurements from the Max Planck Institute (MPI) in Barbados
279 (Weinzierl et al., 2017; Groß et al., 2015; Stevens et al., 2016) provides historical context for
280 aerosol backscatter and depolarization over the island and show structures consistent with the
281 HSRL observations presented here.

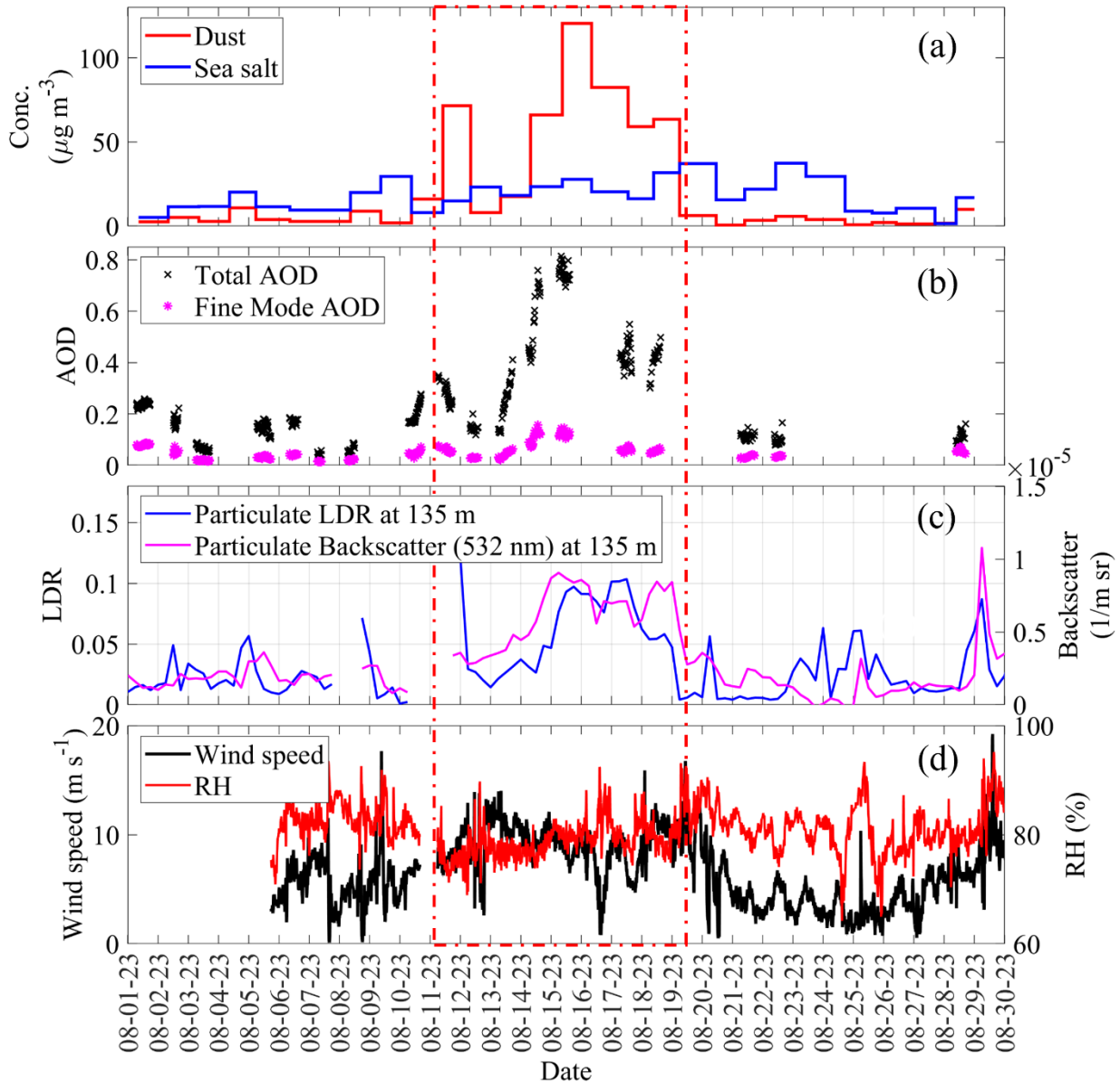
282 For MAGPIE, the SSEC-HSRL was configured to operate in periods of vertical stare,
283 horizontal stare, and vertical scanning from -0.05° to 18° . For the purposes of this paper, we only
284 utilize vertical data. Extraction of light extinction and the lidar ratio within the MABL are
285 performed using the HSRL in one of its side or vertically scanning modes. While a manuscript is
286 under preparation (Fu et al., 2025, in prep.), for the purpose of this paper we can report from its
287 authors that lidar ratios in the MABL’s mixed layer ranged from 15 to 25 sr, and in the SAL was
288 on the order of 35 to 40 sr. Lidar ratios of 15 to 20 sr are consistent with ambient sea salt (RH=
289 70 to 85 % near the surface) and 35 to 40 sr above the MABL for “dry” dust in the less humid
290 SAL (RH= 30 to 50 %).

291 **3. Results and discussion**

292 **3.1. Temporal variability in surface-level aerosol particle chemistry, AOD and lidar
293 depolarization ratios (LDR) during a major dust event**

294 Figure 1 presents a time series of key aerosol properties observed during the August 2023
295 MAGPIE intensive operations period, including surface-level dust and sea salt mass
296 concentrations, aerosol optical depth (AOD), and HSRL-derived particulate linear depolarization
297 ratio (LDR) and particulate backscatter. Over the month, median dust and sea salt concentrations

were 6 ± 32 and $17 \pm 9 \mu\text{g}/\text{m}^3$, respectively; the median columnar AOD was 0.15 ± 0.19 ; and the median LDR at 135 m AMSL was 0.02 ± 0.03 . Notably, a distinct deviation from these baseline values was observed during a period of Saharan dust intrusion occurring between August 11 and 18, 2023. The dust event led to pronounced changes in the chemical composition and physical properties of aerosol particles observed in Barbados, yet the LDR showed little increase. During this period, the dust mass concentration peaked at $120 \mu\text{g}/\text{m}^3$ on August 15, comparable to the concentration measured during the major "Godzilla" dust event of 2020 (Elliott et al., 2024; Mayol-Bracero et al., 2025), while inferred sea salt concentrations based on sodium were $27 \mu\text{g}/\text{m}^3$, representing an upper-limit estimate given the possible contribution of Na from mineral dust. The average dust-to-sea salt mass ratio was ~ 3.4 on dusty days (peaking at 4.8), compared to ~ 0.40 on non-dusty days, indicating a clear dominance of dust in the lower MABL during the dust intrusion event. Total column AOD (550 nm) closely tracked the trend in surface dust mass concentration and peaked at ~ 0.75 on August 15, whereas fine mode AOD remained substantially lower (0.12 ± 0.01 ; Fig. 1b) indicating that the total AOD was predominantly influenced by coarse-mode particles during the dust period. Notably, this event produced one of the highest AOD recorded in Barbados during the month of August over the past decade (Fig. S1).



315

316 Figure 1. Time series plots for (a) dust and sea salt mass concentrations measured from the top of
 317 the BACO tower, (b) AERONET total column and fine mode fraction AODs (at 500 nm), (c)
 318 HSRL- particulate linear depolarization ratio (LDR) and particulate backscatter at 532 nm,
 319 averaged over six hours, and (d) meteorological measurements (RH and wind speed) during the
 320 MAGPIE 2023 campaign. The red dashed box represents the major dust intrusion periods
 321 observed during the campaign.

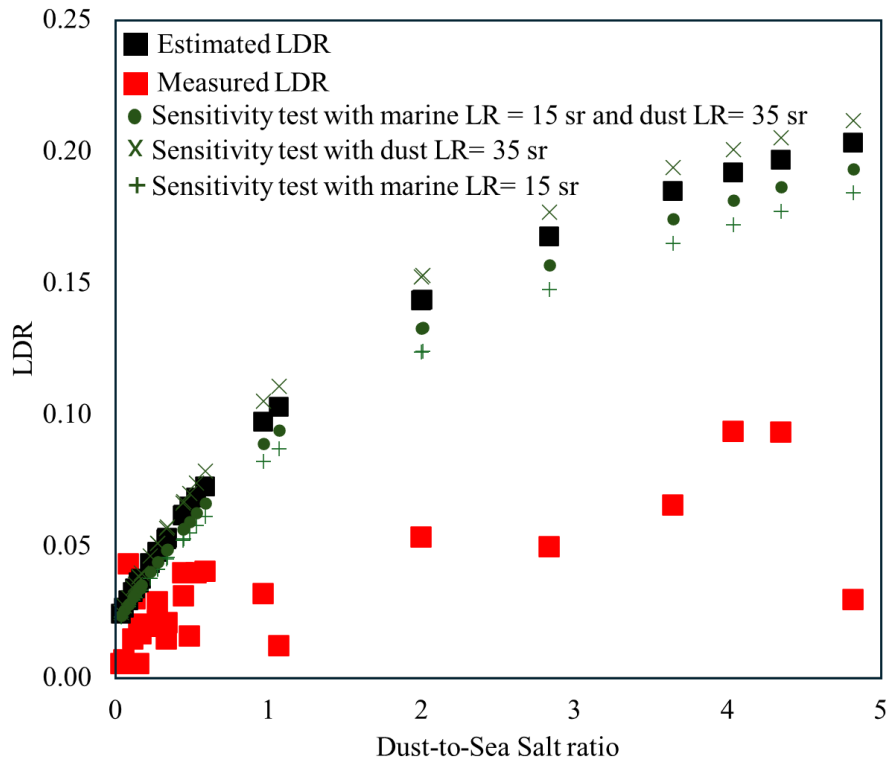
322 Figure 1c presents the time series of the particulate backscatter and LDR at 135 m
323 AMSL, representing conditions near the surface within the lower MABL for comparison with
324 other ground-based measurements. Although an increase in LDR was observed in the lower
325 MABL during the period of pronounced dust loading, the enhancement was surprisingly small,
326 with values of 0.10 or less (Fig. 1c). The finding can be partially explained through scattering
327 physics (e.g., the lidar equation) governing the lidar signals (Hayman and Spuler, 2017). For
328 MAGPIE, the HSRL lidar ratio (LR), the ratio of aerosol extinction (m^{-1}) to backscatter ($m^{-1} sr^{-1}$),
329 was approximately 40 sr for dust and 20 sr for marine aerosols. Because LR is inversely
330 related to the particulate 180° backscatter phase function, a lower LR indicates that marine
331 aerosol particles scatter back approximately twice the amount of energy compared to dust if the
332 marine and dust extinctions are the same. This difference in backscatter directly affects the
333 measured LDR. In a mixed aerosol layer with comparable extinction from dust and marine
334 particles, the backscattered signal, on which the LDR is based, is weighed more strongly toward
335 the marine aerosol contribution (that has a lower LDR).

336 Given that dust concentrations were approximately four times greater than those of sea
337 salt during the peak of the event, we applied a multiple regression approach to estimate the LDR,
338 using Eqn. 2, that incorporated the measured lidar ratio and dust and sea salt concentrations.

339
$$LDRe\text{pected} = \frac{v_{\parallel}^{(d)}}{v_{\parallel}^{(d)} + v_{\parallel}^{(m)}} + \frac{v_{\perp}^{(m)}}{v_{\parallel}^{(d)} + v_{\parallel}^{(m)}} \quad Eqn. 2$$

340 where, $v_{\parallel}^{(d)}$ and $v_{\parallel}^{(m)}$ represent the parallel components, and $v_{\perp}^{(d)}$ and $v_{\perp}^{(m)}$ represent the
341 perpendicular components of the particulate backscatter from dust (“d”) and marine aerosol
342 (“m”) particles, respectively.

343 This analysis yielded an estimated LDR of 0.17 ± 0.03 during the dust peak, ~ 2 times higher
344 than the values observed in Fig 1c in the lower MABL. Details about this calculation and
345 approximations used to derive this estimate are in SI Text S3. Figure 2 shows the relationship
346 between the dust-to-sea salt mass concentration ratio versus the measured HSRL-derived LDR
347 and estimated LDR from the multiple regression approach. We note several caveats to our
348 calculation of the estimated LDR. First, the uncertainty associated with our estimated LDR
349 prediction may be larger than the standard deviation reported, as we did not explicitly account
350 for the full-size distribution of sea salt and dust aerosols. In particular, large particles beyond the
351 upper cut point ($>80 - 100 \mu\text{m}$) of our bulk dust sampler were not captured. While previous
352 studies have shown that some particles of this size can survive trans-Atlantic transport (e.g.,
353 Betzer et al., 1988; Reid et al., 2003a; Barkley et al., 2021), their number concentrations are
354 expected to be substantially lower than those of the particle sizes efficiently collected by the
355 filter sampling used in this study. These coarse particles, which are more efficient at depolarizing
356 incident light due to their irregular shape and size, could contribute significantly to the lidar
357 signal. Their absence from the analysis may lead to an underestimation of the true depolarization
358 potential, especially during intense dust events. Nevertheless, we recognize that other factors
359 may also influence the observed reduction in depolarization. Vertical heterogeneity within the
360 MABL, including overlapping layers of marine and dust aerosols, could further convolute the
361 dust depolarization signal. In addition, inherent limitations in HSRL retrievals, such as signal
362 averaging in optically thin layers or reduced sensitivity near the ocean surface may contribute to
363 the apparent underestimation of LDR.



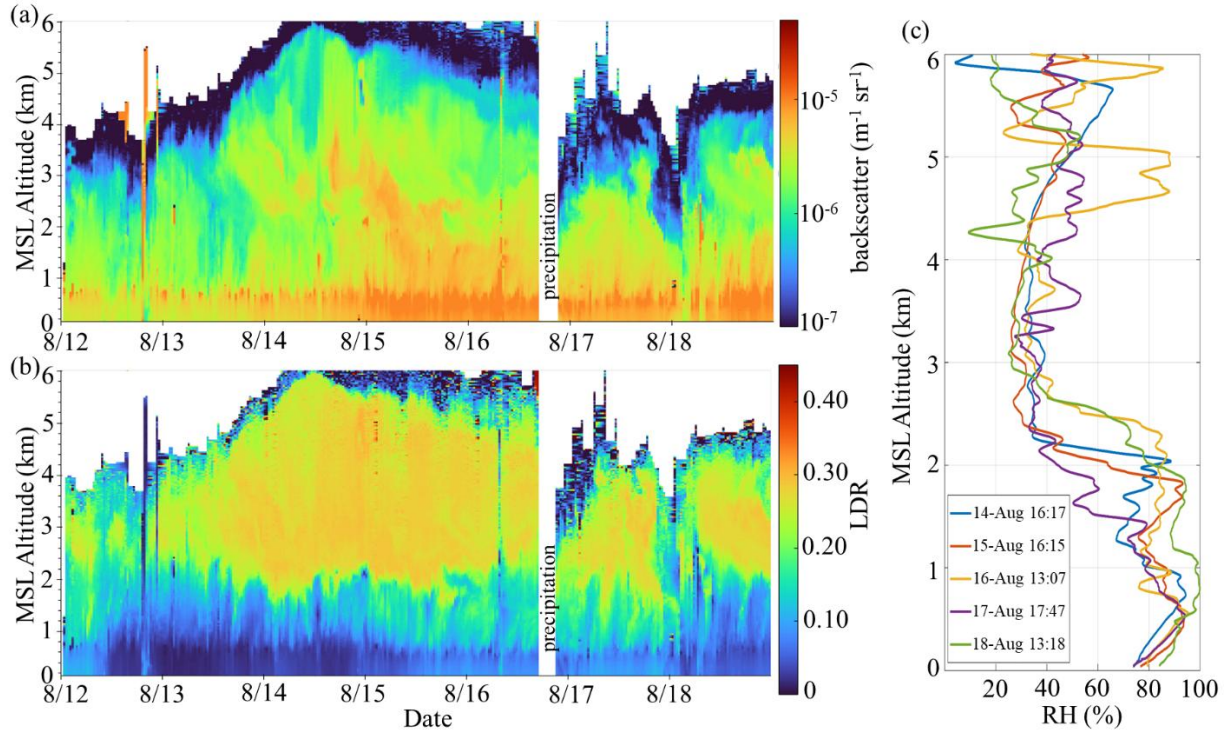
364

365 Figure 2. Relationship between the dust-to-sea salt concentration ratio and HSRL-derived
 366 particulate LDR at 135 m above ground level during the MAGPIE campaign. Red squares
 367 indicate measured LDR values for the full campaign, while black squares represent LDR values
 368 estimated from mass concentrations and lidar ratio weighting during the peak dust event. The
 369 calculated LDR was approximately a factor of two higher than what was observed during the
 370 peak dust event. A sensitivity test was conducted using more conservative lidar ratio values for
 371 dust and marine aerosols (shown as green plus, cross and circle symbols), and in all such cases
 372 the estimated LDR values remained consistently higher than the measured values.

373 Extending our findings in Figure 1c vertically, Figure 3a and b shows the time series of
 374 particulate backscatter and LDR measurements from August 12-18, 2023, at altitude up to 6 km
 375 AMSL. At ~2-6 km AMSL above Ragged Point, measurements of increased particulate
 376 backscatter (shown in Fig 3a) are primarily attributable to increased dust loading within the SAL,

377 as indicated by the concurrent elevated LDR of 0.30 (shown in Fig 3b). This altitude range is
378 consistent with previous studies that have reported the SAL to typically extend from
379 approximately 1.5 to 5.5 km AMSL (Carlson and Prospero, 1972; Groß et al., 2015; Karyampudi
380 and Carlson, 1988; Reid et al., 2003; Weinzierl et al., 2017). The particulate backscatter
381 measurement shown in Fig. 3a highlights high aerosol loading near the surface, consistent with
382 the large concentration of marine particles in the lower MABL. Notably, periods of enhanced
383 backscatter between August 14-16 extending downward from the SAL into the MABL suggest
384 episodes of dust downmixing toward the surface, which are also supported by a concurrent
385 increase in surface dust mass concentrations (Fig. 1).

386 Figure 3c shows the representative vertical distribution of RH during the dusty period of
387 the study, revealing a distinctly moist MABL characterized by RH values exceeding 80%. Such
388 elevated humidity levels are conducive to the hygroscopic growth of aerosol particles, which can
389 increase both particle size and sphericity (Titos et al., 2016). These changes in particle properties
390 caused by hygroscopic growth can further enhance particle backscatter while decreasing the
391 LDR which is visible in the particulate backscatter (Fig. 3a) and LDR (Fig. 3b) measurements
392 below cloud base (~700 m). Thus, under humid MABL conditions, both the LR contrast between
393 dust and marine aerosols and hygroscopicity-driven growth can act together to suppress the
394 observed LDR. However, a key consideration is aerosol mixing state as previous observations
395 have shown limited hygroscopic growth of African dust particles, even at high RH, but
396 substantial growth of dust particles that are internally mixed with other aerosol components
397 including sea spray (Denjean et al., 2015).



398

399 Figure 3. HSRL -measurements for (a) particulate backscatter ($\text{m}^{-1} \text{ sr}^{-1}$) and (b) particulate linear
400 depolarization ratio (LDR) within 6 km AMSL for August 12 -18, 2023. (c) Vertical profiles of
401 relative humidity (RH, %) up to 6 km AMSL from radiosonde launches at Ragged Point on
402 representative days between August 14 and 18, 2023. In panels (a) and (b), periods with
403 particulate backscatter $<10^{-7}$ ($\text{m}^{-1} \text{ sr}^{-1}$) are masked out. The uncertainty associated with the
404 particulate LDR measurements shown in panel (b) is provided in Fig. S2.

405 **3.2. Vertical Gradients in the LDR and aerosol mixing state**

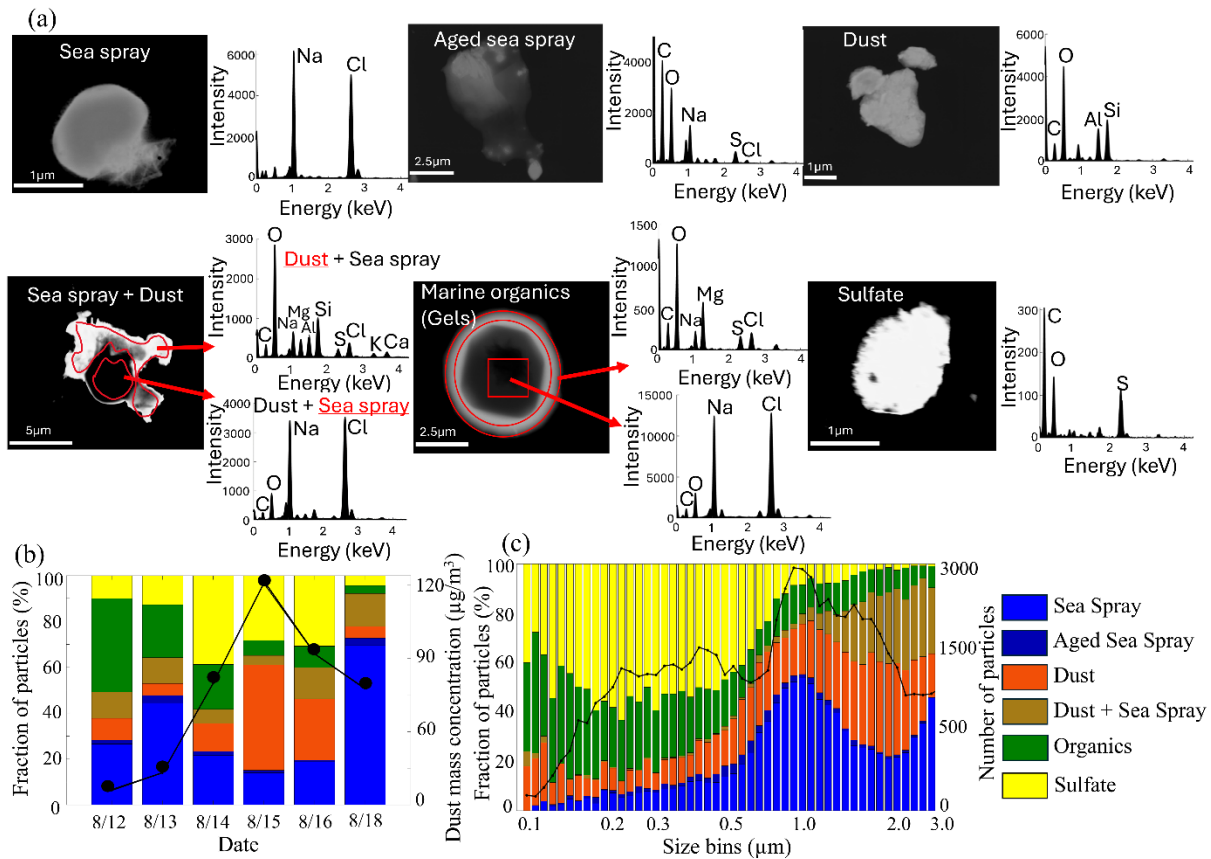
406 A vertical gradient in aerosol particle mixing state was observed during the Saharan dust
407 intrusion, wherein dust is internally mixed with sea spray at the surface and externally mixed
408 aloft. Single-particle chemical composition and morphology analysis revealed a diverse set of
409 particle types with distinct chemistries and morphologies, including mineral dust, sea spray, aged
410 sea spray, internally mixed mineral dust and sea spray, sulfates, and organics (Royer et al., 2023;

411 Ault et al., 2012, 2014). The Methods section describes the particle classification approach and
412 the particle types identified in this study. Detailed chemical composition of the particle types is
413 presented in SI Text S2, representative elemental digital color stack plots used for particle
414 classification are shown in Fig. S3, and representative SEM images and corresponding EDX
415 spectra for each particle class are shown in Fig. 4a.

416 Our single particle results from ground-based samples share several similarities with, but
417 also important differences from, previous studies of Saharan dust transported to the Caribbean.
418 Consistent with Harrison et al., 2022; Krejci et al., 2005; Denjean et al., 2015 and Reid et
419 al., 2003a for the Caribbean, the vast majority of dust particles observed at Barbados during
420 MAGPIE were aluminosilicates, confirming the dominance of this mineralogical class in trans-
421 Atlantic Saharan dust. A prominent feature of the MAGPIE observations was the frequent
422 presence of internally mixed dust and sea spray particles, a phenomenon also documented in
423 earlier Caribbean studies (e.g., Reid et al., 2003a; Aryasree et al., 2024; Royer et al., 2025).
424 Kandler et al. (2018) suggested that such mixing likely occurs locally through turbulent
425 interactions between dust and marine aerosol in the MABL. Our observations are consistent with
426 this mechanism and further suggest that cloud processing may enhance this internal mixing.
427 Similar internally mixed dust and sea spray particles have been reported in other coastal regions,
428 particularly during Asian dust outbreaks (Zhang and Iwasaka, 2004; Zhang et al., 2006; Zhang
429 and Iwasaka, 2001; Zhang et al., 2003), indicating that this mixing process is not unique to the
430 Caribbean but may be characteristic of dust outflows across humid marine environments.

431 Figures 4c and S4 present the average size-resolved chemical composition of ground-
432 level aerosol samples collected during the dust event. A clear compositional shift is observed
433 between submicron and super-micron particles. In the submicron range (particle diameter <

434 1 μm), organic and sulfate aerosol particles were dominant, with median diameters of 0.45 μm
 435 and 0.36 μm , respectively. In contrast, the super-micron size range was dominated by sea spray,
 436 mineral dust, and internally mixed dust and sea spray particles. Externally mixed mineral dust
 437 collected through our impactor had a number median diameter of \sim 1.2 μm , while internally
 438 mixed dust and sea spray particles exhibited larger median diameters of \sim 2.0 μm , likely resulting
 439 from coagulation and condensation processes occurring during dust descent into the MABL
 440 (Kandler et al., 2018). Further, these particles likely become even larger under the high relative
 441 humidity (>80 %) conditions of the MABL consistent with hygroscopic growth (Zieger et al.,
 442 2017). This morphological evolution in internally mixed dust and sea salt particles would
 443 explain, in part, the suppressed LDR during the major dust intrusion event (Bi et al., 2022).

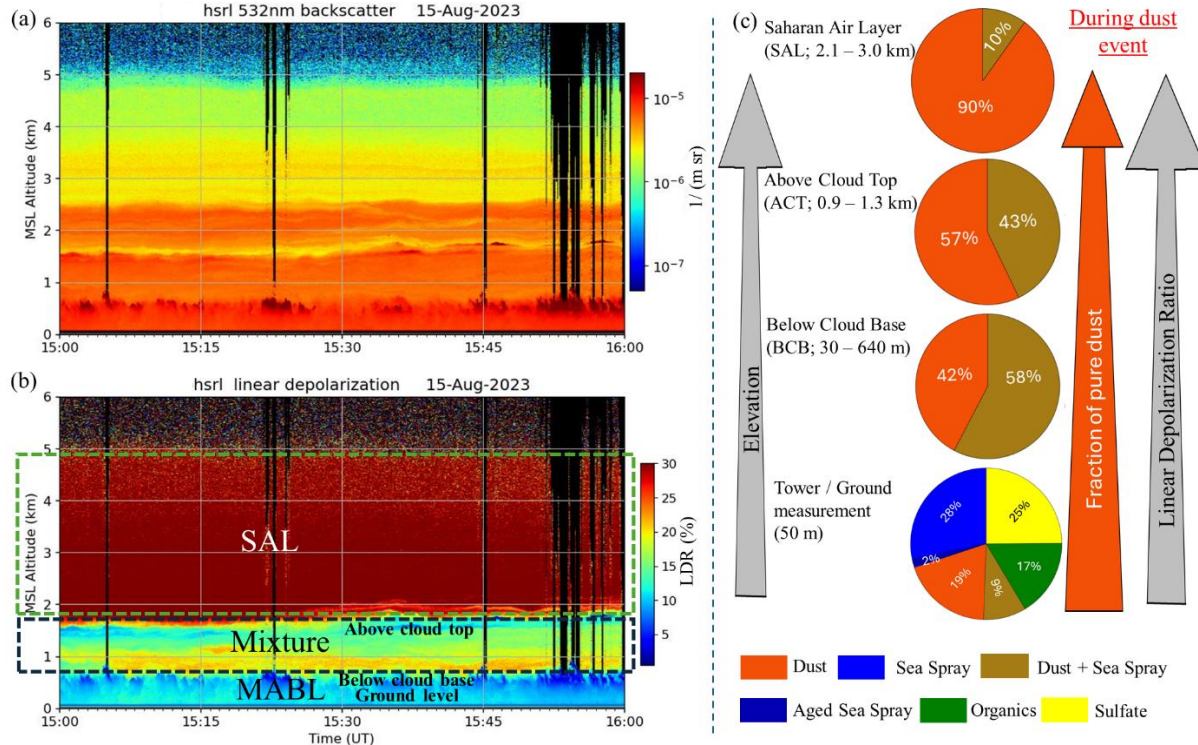


444

445 Figure 4. (a) Representative aerosol particle types observed in surface samples by SEM images
446 (left) and EDX spectra (right) in samples collected during the MAGPIE campaign. (b) Temporal
447 variations in the number fraction of different particle types during the dust event. (c) Number
448 fractions of different particle types plotted as a function of the particle projected area diameter.
449 The black colored line graph in panels (b) & (c) represents dust mass concentration and number
450 of particles, respectively. These plots are generated from the single particle CCSEM/EDX
451 analysis of the in-situ samples collected at the top of the 17 m tower at BACO.

452 To extend this analysis vertically and examine how particle composition varies with
453 altitude, Fig. 5 presents the vertical profile of the number fractions of aerosol particle types,
454 averaged over the samples taken during dusty days, and HSRL data from August 15 (15:00
455 UTC), the day when Barbados experienced the highest ground-level dust concentration (~120
456 $\mu\text{g}/\text{m}^3$). The SAL was predominantly composed of mineral dust particles (90% of the analyzed
457 particles) transported from Northern Africa, and the LDR observed within the SAL (0.30) is
458 attributable to the large fraction of mineral dust present in this layer. Additionally, a transition
459 layer between the SAL and the MABL (labeled as “Mixture” in Fig. 5b) is shown where both sea
460 salt and mineral dust are concurrently present. In the SAL, a fraction of the dust is internally
461 mixed with sea spray particles (10% of the analyzed particles). Below the SAL, between 0.7 km
462 and 1.8 km, LDR values were much smaller and ranged from 0.10 to 0.20, typical for aerosol
463 regimes within the humid MABL where mineral dust particles are mixed with sea spray particles
464 (Gasteiger et al., 2017; Tesche et al., 2011). A comparison of particle composition across
465 altitudes reveals that samples collected above the cloud top contained a slightly higher number
466 fraction of mineral dust (57%) compared to internally mixed dust and sea spray particles (43%).
467 In contrast, below the cloud base, this ratio was reversed, with internally mixed dust and sea

468 spray particles making up 58% of the dust and externally mixed dust 42% of the dust particles
469 suggesting a dynamic, vertical exchange of particles within the MABL. The MABL circulation
470 pattern through clouds is well documented by lidar observations (e.g., from early studies (Kunkel
471 et al., 1977) to more recent work (Reid et al., 2025). Such cloud processing mechanisms likely
472 enhance coagulation while turbulent updrafts promote collisions between sea spray and dust
473 particles (Matsuki et al., 2010). The presence of a substantial fraction of internally mixed dust
474 and sea spray particles above and below cloud base is expected, given that sea salt is a dominant
475 contributor to cloud droplets (Crosbie et al., 2022). The number fraction of mineral dust particles
476 increased substantially in the MABL during periods of intense dust intrusion, with a distinct peak
477 observed on August 15 (Fig. 4b). However, particle composition was more variable at the surface
478 compared to aloft, consistent with the proximity to the ocean increasing the presence of marine
479 aerosol particles including sea salts, organics, and sulfates (Fig. 5c). Further, at altitudes below
480 0.7 km, LDR values were consistently at or below 0.10, commonly taken as being indicative of
481 the dominance of sea spray particles with reduced dust influence (e.g., “Dusty Marine” in the
482 CALIPSO retrievals; Kim et al., 2018).



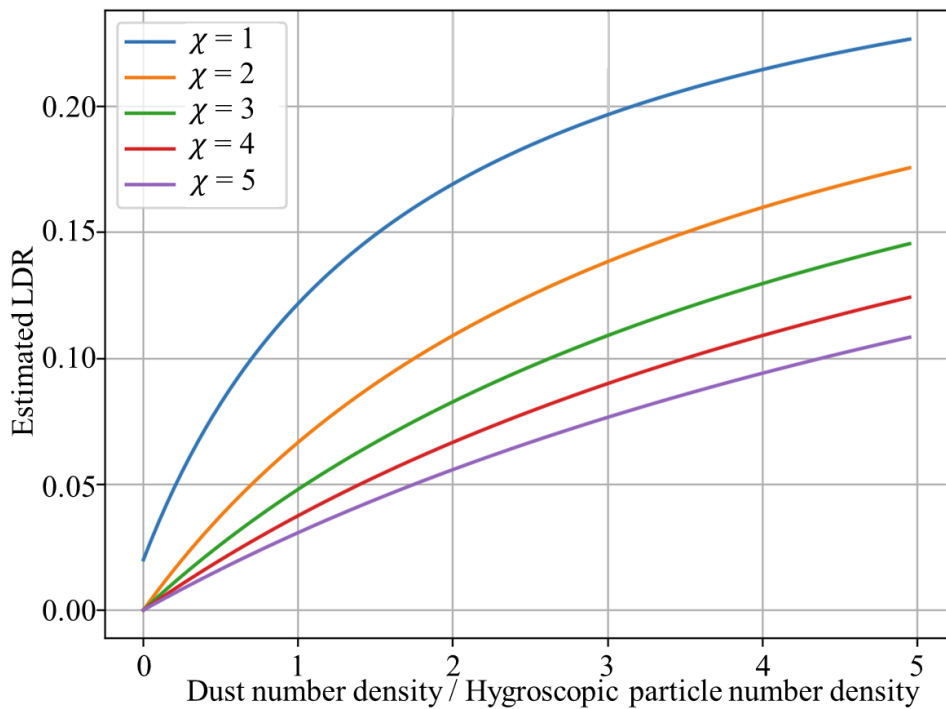
483

484 Figure 5. HSRL scan for (a) particulate backscatter at 532 nm and (b) particulate linear
 485 depolarization ratio within 6 km AMSL for August 15, 2023 (15:00 hrs UTC). (c) Pie charts
 486 showing the number concentration (as a percent) of particle types detected from single particle
 487 analysis at different altitudes: SAL, above cloud top, below cloud top, and ground-based samples
 488 collected atop the BACO tower during the dust event. The altitude range where samples
 489 collected for single particle analysis were taken are indicated in parentheses next to each
 490 corresponding pie chart. Pie charts show that with increased elevation, the fraction of externally
 491 mixed dust increased and the linear depolarization ratio (LDR) from the HSRL measurement
 492 increased during the dust event. The RH vertical profile from a radiosonde launched during this
 493 HSRL observation period shown in panels (a) and (b) is shown as the orange line in Fig. 3c.

494 **3.3. Accounting for Dust Mixing State and Hygroscopic Growth in Predicting the LDR**

495 Prior work by Denjean et al. (2015) showed that externally mixed African dust did not
496 exhibit hygroscopic growth even at high RH (up to 95%), whereas appreciable water uptake
497 occurs primarily when dust is internally mixed with sea spray, a particle type that was
498 prominently observed in our single-particle analysis. Thus, we evaluated how the expected LDR
499 changes when RH-dependent optical weighting is explicitly accounted for by applying a
500 hygroscopic extinction enhancement factor to internally mixed dust and sea spray particles. The
501 detailed discussion of this hygroscopicity dependent calculation is provided in the SI Text S4,
502 and the resulting LDR predictions are shown in Fig. 6. The enhancement factor (χ) represents the
503 marine aerosol extinction enhancement due to the increase in the marine particle cross-sectional
504 area with increasing RH (i.e., hygroscopic growth) (Hänel, 1972, 1976). When this enhancement
505 factor is included, the estimated LDR is further suppressed, consistent with our observations that
506 dust in the moist MABL becomes internally mixed and more spherical when hydrated. This
507 refined estimate improves closure between the measured and predicted depolarization ratios
508 suggesting that hygroscopic growth of internally mixed dust and sea spray particles play a central
509 role in reducing the lidar depolarization signal. Further, simulations of light scattering by
510 nonspherical particles and coated particle systems by Bi et al. (2022) showed that mineral dust
511 particles coated by a hydrated, low refractive index shell (e.g., water, sulfate, or sea salt) can
512 exhibit a strongly suppressed depolarization signal, often approaching values characteristic of
513 spherical particles. This occurs because at high RH the hygroscopic shell grows substantially and
514 dominates the optical response, effectively masking the non-sphericity of the underlying dust
515 core. This coated particle behavior could provide a physical basis for our observations in the
516 humid MABL, where internally mixed dust and sea spray particles observed at RH consistently
517 exceeding 80% produce low LDR values (<0.1) despite high dust mass concentrations and

518 highlights the need to investigate the role of particle composition and mixing state in modulating
 519 depolarization signals. Overall, these observations suggest that the reduced LDR values in the
 520 MABL are likely explained, in part, by internally mixed dust and hydrated sea spray particles in
 521 the presence of high humidity, resulting in hydrated, more spherical and hence less depolarizing
 522 particles.



523
 524 Figure 6. Relationship between estimated LDR and dust-to-hygrosopic particle number density
 525 ratio as a function of marine aerosol extinction enhancement factor (χ) due to hygroscopic
 526 growth. The estimates are based on the observed HSRL-LDR for dry dust particles as 0.3 and LR
 527 for dry dust particles as 35 sr and the observed average ratio of cross-sectional area of internally
 528 mixed dust and sea spray particles to that of externally mixed dust particles as 2.7, derived from
 529 CCSEM/EDX single-particle analysis of surface samples collected at BACO. Cross-sectional
 530 areas were calculated using the respective median diameters measured for each particle type.

531

532 **4. Conclusions and Atmospheric Implications**

533 Single-particle analysis conducted during the MAGPIE campaign revealed that Saharan
534 dust particles in the MABL are physically and chemically distinct from dust within the SAL
535 aloft. Our results show that in the lower, humid MABL, dust becomes internally mixed with sea
536 spray resulting in potentially enhanced hygroscopicity compared to externally mixed dust in
537 agreement with prior studies investigating the hygroscopicity of transported African dust
538 (Denjean et al., 2015). These changes, in part, suppress the dust's depolarization (being more
539 spherical) signal and complicate its identification by lidar. Despite peak dust loading at BACO
540 (AOD \sim 0.75; surface dust \sim 120 $\mu\text{g}/\text{m}^3$), HSRL observations showed that LDR values in the
541 lower MABL remained mostly below 0.10, a range typically associated with spherical marine
542 aerosols, even though dust concentrations were \sim 4.8 times higher than sea salt. This discrepancy
543 is further explained by differences in the scattering (lidar ratio) of dust and marine aerosols,
544 where dust backscatters half the energy per extinction cross-section (lidar ratio) compared to
545 marine aerosols which lowers the depolarization measurement. These combined effects of
546 morphological transformation and different lidar ratios reduce the dust signature in
547 depolarization-based retrievals, complicating its detection and quantification near the surface.
548 The resulting underestimation of surface-level dust by lidar-based depolarization retrievals is of
549 particular concern especially during high-dust events like the one observed during this study,
550 where surface particulate matter (PM) exceeded WHO guidelines for PM₁₀ of 45 $\mu\text{g}/\text{m}^3$ (World
551 Health Organization, 2021) by a factor of nearly three. Moreover, it may help explain similar
552 discrepancies between lidar observations and in situ measurements in other regions where dust is
553 modified through interactions with marine aerosols.

554 More broadly, these results highlight the importance of integrating vertically resolved
555 lidar data with in-situ single-particle analysis and surface aerosol mass concentrations to improve
556 the interpretation of lidar observations in dust-affected regions. Such integrated approaches are
557 essential because LDR is widely used in satellite retrieval algorithms and atmospheric models to
558 estimate dust volume and mass fractions, calculate dust-related radiative forcing, estimate dust
559 contribution to cloud condensation and ice nucleation profiles, estimate dust deposition to
560 receptor ecosystems, and predict surface air quality (Meloni et al., 2018; Haarig et al., 2017;
561 Müller et al., 2010, 2012; Yang et al., 2012; Marinou et al., 2017; Proestakis et al., 2018; Adebiyi
562 et al., 2023; Mahowald et al., 2005). Without such integrated observations, satellite retrievals and
563 forecasting systems may significantly underestimate dust impacts near the surface, where they
564 matter most for air quality and biogeochemical feedback.

565 While our results demonstrate that single wavelength depolarization can underestimate
566 near surface dust under humid, mixed aerosol conditions, we emphasize that more advanced
567 remote sensing approaches can mitigate these limitations. Multi-wavelength HSRL observations,
568 including backscatter at 532, and 1064 nm and corresponding color ratio and depolarization
569 metrics, provide additional degrees of freedom for discriminating dust from hydrated marine
570 aerosol particles. In fact, recent upgrades by the SSEC HSRL team have produced the first
571 calibrated 1064 nm HSRL system, that is aimed at being deployed in future studies. These multi-
572 spectral measurements would enable color ratio signatures characteristic of dust to be detected
573 even when LDR is low, thereby providing a remote sensing pathway to constrain surface dust
574 loading. Validating these multi-spectral retrievals requires independent constraints on aerosol
575 composition and morphology. The vertically resolved single particle measurements presented
576 here provide validation of how dust properties change as they mix with sea spray. Thus, rather

577 than diminishing the utility of lidar, our results highlight the importance of integrating advanced
578 multi-wavelength lidar products with targeted in-situ observations to improve the accuracy of
579 surface dust estimates in marine environments.

580 **Data Availability**

581 Dust and sea salt mass concentration data and number counts of particle types detected by
582 CCSEM/EDX is publicly available in the University of Miami data repository
583 (<https://doi.org/10.17604/1427-0558>).

584 The HSRL data can be accessed through the University of Wisconsin-Madison SSEC repository
585 at https://hsrl.ssec.wisc.edu/by_site/37/bscat/2025/04/.

586 The NASA AERONET data can be accessed through <https://aeronet.gsfc.nasa.gov>.

587 **Author Contribution**

588 Conceptualization of this work was done by SS, RJH, JSR, and CJG. JSR posed the initial
589 hypothesis and designed the data collection strategy. Collection of samples was conducted by SS,
590 WJM, ZB, IR, EE, JSR, EB, ADO, RCL, AA, DB, EAR, JRP, AB, RY, QW, TE, EL, MLP, and
591 CJG, while analysis was done by SS, HEE, NNL, ZC, SC, and RA. The development of method
592 used in this work was done by SS, REH, WJM, EE, JSR, and CJG. Instrumentation used to
593 conduct this work was provided by REH, SC, MLP, and CJG. Formal analysis of data was
594 performed by SS, WJM, and JSR. EE performed the optical calculations of expected LDR.
595 Validation of data products was performed by SS, RJH, WJM, JSR, AA, and CJG. Data
596 visualization was performed by SS. Supervision and project administration duties were done by
597 RJH, JSR, and CJG. SS wrote the original draft for publication, and all the co-authors reviewed
598 and edited this work.

599 **Competing Interests**

600 The contact author has declared that none of the authors has any competing interests.

601 **Acknowledgements**

602 We thank the family of HC Manning and the Herbert C Manning Trust for providing access to
603 their land at Ragged Point in Barbados. We thank Jeremy Bougoure at EMSL for his help with
604 the Au sputter coating of our filter samples. We thank Dr. Konrad Kandler and the other
605 reviewers for their constructive and insightful comments, which substantially improved the
606 clarity and rigor of this manuscript.

607 **Financial Support**

608 CJG and SS acknowledge the Office of Naval Research (ONR) grants N00014-23-1-2861 and
609 N000142512003 and NSF MRI grant 2215875. A portion of this research was performed on
610 project awards ([10.46936/lser.proj.2021.51900/60000361](https://doi.org/10.46936/lser.proj.2021.51900/60000361) and
611 <https://doi.org/10.46936/ltds.proj.2023.61072/60012372>) from the Environmental Molecular
612 Sciences Laboratory, a DOE Office of Science User Facility sponsored by the Biological and
613 Environmental Research program. REH, WJM, ZB, IR and EE were supported under ONR grant
614 N000142412736 and N00014-21-1-2130. JSR and EAR were supported under ONR grant
615 O2507-017-017-112205. AB was supported under ONR grant N0001423WX01787. QW, JRP
616 and RY were supported under ONR grant N0001424WX02429. APA acknowledges support from
617 ONR grant N000142512003 and DOE grant DE-SC0025196.

618 **References**

619 Adams, A. M., Prospero, J. M., and Zhang, C.: CALIPSO-Derived Three-Dimensional Structure
620 of Aerosol over the Atlantic Basin and Adjacent Continents, *J. Clim.*, 25, 6862–6879,
621 <https://doi.org/10.1175/JCLI-D-11-00672.1>, 2012.

622 Adebiyi, A., Kok, J. F., Murray, B. J., Ryder, C. L., Stuut, J.-B. W., Kahn, R. A., Knippertz, P.,
623 Formenti, P., Mahowald, N. M., Pérez García-Pando, C., Klose, M., Ansmann, A., Samset, B.
624 H., Ito, A., Balkanski, Y., Di Biagio, C., Romanias, M. N., Huang, Y., and Meng, J.: A review of
625 coarse mineral dust in the Earth system, *Aeolian Res.*, 60, 100849,
626 <https://doi.org/10.1016/j.aeolia.2022.100849>, 2023.

627 Andreae, M. O., Charlson, R. J., Bruynseels, F., Storms, H., Van Grieken, R., and Maenhaut, W.:
628 Internal Mixture of Sea Salt, Silicates, and Excess Sulfate in Marine Aerosols, *Science* (80-.),,
629 232, 1620–1623, <https://doi.org/10.1126/science.232.4758.1620>, 1986.

630 Aryasree, S., Kandler, K., Benker, N., Walser, A., Tipka, A., Dollner, M., Seibert, P., and
631 Weinzierl, B.: Vertical Variability in morphology, chemistry and optical properties of the
632 transported Saharan air layer measured from Cape Verde and the Caribbean, *R. Soc. Open Sci.*,
633 11, <https://doi.org/10.1098/rsos.231433>, 2024.

634 Ault, A. P., Peters, T. M., Sawvel, E. J., Casuccio, G. S., Willis, R. D., Norris, G. A., and
635 Grassian, V. H.: Single-Particle SEM-EDX Analysis of Iron-Containing Coarse Particulate
636 Matter in an Urban Environment: Sources and Distribution of Iron within Cleveland, Ohio,
637 *Environ. Sci. Technol.*, 46, 4331–4339, <https://doi.org/10.1021/es204006k>, 2012.

638 Ault, A. P., Guasco, T. L., Ryder, O. S., Baltrusaitis, J., Cuadra-Rodriguez, L. A., Collins, D. B.,
639 Ruppel, M. J., Bertram, T. H., Prather, K. A., and Grassian, V. H.: Inside versus Outside: Ion
640 Redistribution in Nitric Acid Reacted Sea Spray Aerosol Particles as Determined by Single
641 Particle Analysis, *J. Am. Chem. Soc.*, 135, 14528–14531, <https://doi.org/10.1021/ja407117x>,
642 2013.

643 Ault, A. P., Guasco, T. L., Baltrusaitis, J., Ryder, O. S., Trueblood, J. V., Collins, D. B., Ruppel,
644 M. J., Cuadra-Rodriguez, L. A., Prather, K. A., and Grassian, V. H.: Heterogeneous Reactivity of
645 Nitric Acid with Nascent Sea Spray Aerosol: Large Differences Observed between and within
646 Individual Particles, *J. Phys. Chem. Lett.*, 5, 2493–2500, <https://doi.org/10.1021/jz5008802>,
647 2014.

648 Barkley, A. E., Olson, N. E., Prospero, J. M., Gatineau, A., Panechou, K., Maynard, N. G.,
649 Blackwelder, P., China, S., Ault, A. P., and Gaston, C. J.: Atmospheric Transport of North
650 African Dust-Bearing Supermicron Freshwater Diatoms to South America: Implications for Iron
651 Transport to the Equatorial North Atlantic Ocean, *Geophys. Res. Lett.*, 48,
652 <https://doi.org/10.1029/2020GL090476>, 2021.

653 Betzer, P. R., Carder, K. L., Duce, R. A., Merrill, J. T., Tindale, N. W., Uematsu, M., Costello,
654 D. K., Young, R. W., Feely, R. A., Breland, J. A., Bernstein, R. E., and Greco, A. M.: Long-
655 range transport of giant mineral aerosol particles, *Nature*, 336, 568–571,
656 <https://doi.org/10.1038/336568a0>, 1988.

657 Bi, L., Wang, Z., Han, W., Li, W., and Zhang, X.: Computation of Optical Properties of Core-
658 Shell Super-Spheroids Using a GPU Implementation of the Invariant Imbedding T-Matrix
659 Method, *Front. Remote Sens.*, 3, <https://doi.org/10.3389/frsen.2022.903312>, 2022.

660 Bondy, A. L., Bonanno, D., Moffet, R. C., Wang, B., Laskin, A., and Ault, A. P.: The diverse
661 chemical mixing state of aerosol particles in the southeastern United States, *Atmos. Chem. Phys.*,
662 18, 12595–12612, <https://doi.org/10.5194/acp-18-12595-2018>, 2018.

663 Burton, S. P., Ferrare, R. A., Hostetler, C. A., Hair, J. W., Rogers, R. R., Obland, M. D., Butler,

664 C. F., Cook, A. L., Harper, D. B., and Froyd, K. D.: Aerosol classification using airborne High
665 Spectral Resolution Lidar measurements – methodology and examples, *Atmos. Meas. Tech.*, 5,
666 73–98, <https://doi.org/10.5194/amt-5-73-2012>, 2012.

667 Burton, S. P., Hair, J. W., Kahnert, M., Ferrare, R. A., Hostetler, C. A., Cook, A. L., Harper, D.
668 B., Berkoff, T. A., Seaman, S. T., Collins, J. E., Fenn, M. A., and Rogers, R. R.: Observations of
669 the spectral dependence of linear particle depolarization ratio of aerosols using NASA Langley
670 airborne High Spectral Resolution Lidar, *Atmos. Chem. Phys.*, 15, 13453–13473,
671 <https://doi.org/10.5194/acp-15-13453-2015>, 2015.

672 Carlson, T. N. and Prospero, J. M.: The Large-Scale Movement of Saharan Air Outbreaks over
673 the Northern Equatorial Atlantic, *J. Appl. Meteorol. Clim.*, 11, 283–297,
674 [https://doi.org/https://doi.org/10.1175/1520-0450\(1972\)011<0283:TLSMOS>2.0.CO;2](https://doi.org/https://doi.org/10.1175/1520-0450(1972)011<0283:TLSMOS>2.0.CO;2), 1972.

675 Casuccio, G. S., Janocko, P. B., Lee, R. J., Kelly, J. F., Dattner, S. L., and Mgebroff, J. S.: The
676 Use of Computer Controlled Scanning Electron Microscopy in Environmental Studies, *J. Air
677 Pollut. Control Assoc.*, 33, 937–943, <https://doi.org/10.1080/00022470.1983.10465674>, 1983.

678 Chin, W.-C., Orellana, M. V., and Verdugo, P.: Spontaneous assembly of marine dissolved
679 organic matter into polymer gels, *Nature*, 391, 568–572, <https://doi.org/10.1038/35345>, 1998.

680 Crosbie, E., Ziembka, L. D., Shook, M. A., Robinson, C. E., Winstead, E. L., Thornehill, K. L.,
681 Braun, R. A., MacDonald, A. B., Stahl, C., Sorooshian, A., van den Heever, S. C., DiGangi, J.
682 P., Diskin, G. S., Woods, S., Bañaga, P., Brown, M. D., Gallo, F., Hilario, M. R. A., Jordan, C.
683 E., Leung, G. R., Moore, R. H., Sanchez, K. J., Shingler, T. J., and Wiggins, E. B.: Measurement
684 report: Closure analysis of aerosol–cloud composition in tropical maritime warm convection,
685 *Atmos. Chem. Phys.*, 22, 13269–13302, <https://doi.org/10.5194/acp-22-13269-2022>, 2022.

686 Denjean, C., Caquineau, S., Desboeufs, K., Laurent, B., Maille, M., Quiñones Rosado, M.,
687 Vallejo, P., Mayol-Bracero, O. L., and Formenti, P.: Long-range transport across the Atlantic in
688 summertime does not enhance the hygroscopicity of African mineral dust, *Geophys. Res. Lett.*,
689 42, 7835–7843, <https://doi.org/10.1002/2015GL065693>, 2015.

690 Elliott, H. E., Popendorf, K. J., Blades, E., Royer, H. M., Pollier, C. G. L., Oehlert, A. M.,
691 Kukkadapu, R., Ault, A., and Gaston, C. J.: Godzilla mineral dust and La Soufrière volcanic ash
692 fallout immediately stimulate marine microbial phosphate uptake, *Front. Mar. Sci.*, 10,
693 <https://doi.org/10.3389/fmars.2023.1308689>, 2024.

694 Eloranta, E. W., Razenkov, I. A., Hedrick, J., and Garcia, J. P.: The design and construction of
695 an airborne high spectral resolution lidar, in: *IEEE Aerospace Conference Proceedings*,
696 <https://doi.org/10.1109/AERO.2008.4526390>, 2008.

697 Freudenthaler, V., Esselborn, M., Wiegner, M., Heese, B., Tesche, M., Ansmann, A., Müller, D.,
698 Althausen, D., Wirth, M., Fix, A., Ehret, G., Knippertz, P., Toledano, C., Gasteiger, J.,
699 Garhammer, M., and Seefeldner, M.: Depolarization ratio profiling at several wavelengths in
700 pure Saharan dust during SAMUM 2006, *Tellus B Chem. Phys. Meteorol.*, 61, 165,
701 <https://doi.org/10.1111/j.1600-0889.2008.00396.x>, 2009.

702 Gasteiger, J., Groß, S., Sauer, D., Haarig, M., Ansmann, A., and Weinzierl, B.: Particle settling
703 and vertical mixing in the Saharan Air Layer as seen from an integrated model, lidar, and in situ
704 perspective, *Atmos. Chem. Phys.*, 17, 297–311, <https://doi.org/10.5194/acp-17-297-2017>, 2017.

705 Gaston, C. J., Furutani, H., Guazzotti, S. A., Coffee, K. R., Bates, T. S., Quinn, P. K., Aluwihare,

706 L. I., Mitchell, B. G., and Prather, K. A.: Unique ocean-derived particles serve as a proxy for
707 changes in ocean chemistry, *J. Geophys. Res.*, 116, D18310,
708 <https://doi.org/10.1029/2010JD015289>, 2011.

709 Gaston, C. J., Prospero, J. M., Foley, K., Pye, H. O. T., Custals, L., Blades, E., Sealy, P., and
710 Christie, J. A.: Diverging trends in aerosol sulfate and nitrate measured in the remote North
711 Atlantic in Barbados are attributed to clean air policies, African smoke, and anthropogenic
712 emissions, *Atmos. Chem. Phys.*, 24, 8049–8066, <https://doi.org/10.5194/acp-24-8049-2024>,
713 2024.

714 Giles, D. M., Sinyuk, A., Sorokin, M. G., Schafer, J. S., Smirnov, A., Slutsker, I., Eck, T. F.,
715 Holben, B. N., Lewis, J. R., Campbell, J. R., Welton, E. J., Korkin, S. V., and Lyapustin, A. I.:
716 Advancements in the Aerosol Robotic Network (AERONET) Version 3 database – automated
717 near-real-time quality control algorithm with improved cloud screening for Sun photometer
718 aerosol optical depth (AOD) measurements, *Atmos. Meas. Tech.*, 12, 169–209,
719 <https://doi.org/10.5194/amt-12-169-2019>, 2019.

720 Groß, S., Freudenthaler, V., Schepanski, K., Toledano, C., Schäfler, A., Ansmann, A., and
721 Weinzierl, B.: Optical properties of long-range transported Saharan dust over Barbados as
722 measured by dual-wavelength depolarization Raman lidar measurements, *Atmos. Chem. Phys.*,
723 15, 11067–11080, <https://doi.org/10.5194/acp-15-11067-2015>, 2015.

724 Groß, S., Gasteiger, J., Freudenthaler, V., Müller, T., Sauer, D., Toledano, C., and Ansmann, A.:
725 Saharan dust contribution to the Caribbean summertime boundary layer – a lidar study during
726 SALTRACE, *Atmos. Chem. Phys.*, 16, 11535–11546, <https://doi.org/10.5194/acp-16-11535-2016>, 2016.

727 Haarig, M., Ansmann, A., Althausen, D., Klepel, A., Groß, S., Freudenthaler, V., Toledano, C.,
728 Mamouri, R.-E., Farrell, D. A., Prescod, D. A., Marinou, E., Burton, S. P., Gasteiger, J.,
729 Engelmann, R., and Baars, H.: Triple-wavelength depolarization-ratio profiling of Saharan dust
730 over Barbados during SALTRACE in 2013 and 2014, *Atmos. Chem. Phys.*, 17, 10767–10794,
731 <https://doi.org/10.5194/acp-17-10767-2017>, 2017.

732 Hand, V. L., Capes, G., Vaughan, D. J., Formenti, P., Haywood, J. M., and Coe, H.: Evidence of
733 internal mixing of African dust and biomass burning particles by individual particle analysis
734 using electron beam techniques, *J. Geophys. Res. Atmos.*, 115,
735 <https://doi.org/10.1029/2009JD012938>, 2010.

736 Hänel, G.: Computation of the extinction of visible radiation by atmospheric aerosol particles as
737 a function of the relative humidity, based upon measured properties, *J. Aerosol Sci.*, 3, 377–386,
738 [https://doi.org/10.1016/0021-8502\(72\)90092-4](https://doi.org/10.1016/0021-8502(72)90092-4), 1972.

739 Hänel, G.: The Single-Scattering Albedo of Atmospheric Aerosol Particles as a Function of
740 Relative Humidity, *J. Atmos. Sci.*, 33, 1120–1124, [https://doi.org/10.1175/1520-0469\(1976\)033<1120:TSSAOA>2.0.CO;2](https://doi.org/10.1175/1520-0469(1976)033<1120:TSSAOA>2.0.CO;2), 1976.

741 Harrison, A. D., O’Sullivan, D., Adams, M. P., Porter, G. C. E., Blades, E., Brathwaite, C.,
742 Chewitt-Lucas, R., Gaston, C., Hawker, R., Krüger, O. O., Neve, L., Pöhlker, M. L., Pöhlker, C.,
743 Pöschl, U., Sanchez-Marroquin, A., Sealy, A., Sealy, P., Tarn, M. D., Whitehall, S., McQuaid, J.,
744 B., Carslaw, K. S., Prospero, J. M., and Murray, B. J.: The ice-nucleating activity of African
745 mineral dust in the Caribbean boundary layer, *Atmos. Chem. Phys.*, 22, 9663–9680,
746 <https://doi.org/10.5194/acp-22-9663-2022>, 2022.

747

748

749 Hayman, M. and Spuler, S.: Demonstration of a diode-laser-based high spectral resolution lidar
750 (HSRL) for quantitative profiling of clouds and aerosols, *Opt. Express*, 25, A1096,
751 <https://doi.org/10.1364/OE.25.0A1096>, 2017.

752 Holben, B. N., Eck, T. F., Slutsker, I., Tanré, D., Buis, J. P., Setzer, A., Vermote, E., Reagan, J.
753 A., Kaufman, Y. J., Nakajima, T., Lavenu, F., Jankowiak, I., and Smirnov, A.: AERONET—A
754 Federated Instrument Network and Data Archive for Aerosol Characterization, *Remote Sens.
755 Environ.*, 66, 1–16, [https://doi.org/10.1016/S0034-4257\(98\)00031-5](https://doi.org/10.1016/S0034-4257(98)00031-5), 1998.

756 Huang, X., Yang, P., Kattawar, G., and Liou, K.-N.: Effect of mineral dust aerosol aspect ratio
757 on polarized reflectance, *J. Quant. Spectrosc. Radiat. Transf.*, 151, 97–109,
758 <https://doi.org/10.1016/j.jqsrt.2014.09.014>, 2015.

759 Kalashnikova, O. V., Garay, M. J., Martonchik, J. V., and Diner, D. J.: MISR Dark Water
760 aerosol retrievals: operational algorithm sensitivity to particle non-sphericity, *Atmos. Meas.
761 Tech.*, 6, 2131–2154, <https://doi.org/10.5194/amt-6-2131-2013>, 2013.

762 Kandler, K., Schneiders, K., Ebert, M., Hartmann, M., Weinbruch, S., Prass, M., and Pöhlker, C.:
763 Composition and mixing state of atmospheric aerosols determined by electron microscopy:
764 method development and application to aged Saharan dust deposition in the Caribbean boundary
765 layer, *Atmos. Chem. Phys.*, 18, 13429–13455, <https://doi.org/10.5194/acp-18-13429-2018>, 2018.

766 Karyampudi, V. M. and Carlson, T. N.: Analysis and Numerical Simulations of the Saharan Air
767 Layer and Its Effect on Easterly Wave Disturbances, *J. Atmos. Sci.*, 45, 3102–3136,
768 [https://doi.org/10.1175/1520-0469\(1988\)045<3102:AANSOT>2.0.CO;2](https://doi.org/10.1175/1520-0469(1988)045<3102:AANSOT>2.0.CO;2), 1988.

769 Karyampudi, V. M., Palm, S. P., Reagen, J. A., Fang, H., Grant, W. B., Hoff, R. M., Moulin, C.,
770 Pierce, H. F., Torres, O., Browell, E. V., and Melfi, S. H.: Validation of the Saharan Dust Plume
771 Conceptual Model Using Lidar, Meteosat, and ECMWF Data, *Bull. Am. Meteorol. Soc.*, 80,
772 1045–1075, [https://doi.org/10.1175/1520-0477\(1999\)080<1045:VOTSDP>2.0.CO;2](https://doi.org/10.1175/1520-0477(1999)080<1045:VOTSDP>2.0.CO;2), 1999.

773 Kim, D. S., Hopke, P. K., Massart, D. L., Kaufman, L., and Casuccio, G. S.: Multivariate
774 analysis of CCSEM auto emission data, *Sci. Total Environ.*, 59, 141–155,
775 [https://doi.org/10.1016/0048-9697\(87\)90438-4](https://doi.org/10.1016/0048-9697(87)90438-4), 1987.

776 Kim, M.-H., Omar, A. H., Tackett, J. L., Vaughan, M. A., Winker, D. M., Trepte, C. R., Hu, Y.,
777 Liu, Z., Poole, L. R., Pitts, M. C., Kar, J., and Magill, B. E.: The CALIPSO version 4 automated
778 aerosol classification and lidar ratio selection algorithm, *Atmos. Meas. Tech.*, 11, 6107–6135,
779 <https://doi.org/10.5194/amt-11-6107-2018>, 2018.

780 Koehler, K. A., Kreidenweis, S. M., DeMott, P. J., Prenni, A. J., and Petters, M. D.: Potential
781 impact of Owens (dry) Lake dust on warm and cold cloud formation, *J. Geophys. Res. Atmos.*,
782 112, <https://doi.org/10.1029/2007JD008413>, 2007.

783 Kong, S., Sato, K., and Bi, L.: Lidar Ratio–Depolarization Ratio Relations of Atmospheric Dust
784 Aerosols: The Super-Spheroid Model and High Spectral Resolution Lidar Observations, *J.
785 Geophys. Res. Atmos.*, 127, <https://doi.org/10.1029/2021JD035629>, 2022.

786 Krejci, R., Ström, J., de Reus, M., and Sahle, W.: Single particle analysis of the accumulation
787 mode aerosol over the northeast Amazonian tropical rain forest, Surinam, South America,
788 *Atmos. Chem. Phys.*, 5, 3331–3344, <https://doi.org/10.5194/acp-5-3331-2005>, 2005.

789 Krueger, B. J., Grassian, V. H., Cowin, J. P., and Laskin, A.: Heterogeneous chemistry of

790 individual mineral dust particles from different dust source regions: the importance of particle
791 mineralogy, *Atmos. Environ.*, 38, 6253–6261, <https://doi.org/10.1016/j.atmosenv.2004.07.010>,
792 2004.

793 Kunkel, K. E., Eloranta, E. W., and Shipley, S. T.: Lidar Observations of the Convective
794 Boundary Layer, *J. Appl. Meteorol.*, 16, 1306–1311, [https://doi.org/10.1175/1520-0450\(1977\)016<1306:LOOTCB>2.0.CO;2](https://doi.org/10.1175/1520-0450(1977)016<1306:LOOTCB>2.0.CO;2), 1977.

795 Levin, Z., Teller, A., Ganor, E., and Yin, Y.: On the interactions of mineral dust, sea-salt
796 particles, and clouds: A measurement and modeling study from the Mediterranean Israeli Dust
797 Experiment campaign, *J. Geophys. Res. Atmos.*, 110, <https://doi.org/10.1029/2005JD005810>,
798 2005.

799 Li-Jones, X., Maring, H. B., and Prospero, J. M.: Effect of relative humidity on light scattering
800 by mineral dust aerosol as measured in the marine boundary layer over the tropical Atlantic
801 Ocean, *J. Geophys. Res. Atmos.*, 103, 31113–31121, <https://doi.org/10.1029/98JD01800>, 1998.

802 Li, C., Li, J., Dubovik, O., Zeng, Z.-C., and Yung, Y. L.: Impact of Aerosol Vertical Distribution
803 on Aerosol Optical Depth Retrieval from Passive Satellite Sensors, *Remote Sens.*, 12, 1524,
804 <https://doi.org/10.3390/rs12091524>, 2020.

805 Mahowald, N. M., Baker, A. R., Bergametti, G., Brooks, N., Duce, R. A., Jickells, T. D.,
806 Kubilay, N., Prospero, J. M., and Tegen, I.: Atmospheric global dust cycle and iron inputs to the
807 ocean, *Global Biogeochem. Cycles*, 19, <https://doi.org/10.1029/2004GB002402>, 2005.

808 Marinou, E., Amiridis, V., Binietoglou, I., Tsikerdekis, A., Solomos, S., Proestakis, E., Konsta,
809 D., Papagiannopoulos, N., Tsekeri, A., Vlastou, G., Zanis, P., Balis, D., Wandinger, U., and
810 Ansmann, A.: Three-dimensional evolution of Saharan dust transport towards Europe based on a
811 9-year EARLINET-optimized CALIPSO dataset, *Atmos. Chem. Phys.*, 17, 5893–5919,
812 <https://doi.org/10.5194/acp-17-5893-2017>, 2017.

813 Matsuki, A., Schwarzenboeck, A., Venzac, H., Laj, P., Crumeyrolle, S., and Gomes, L.: Cloud
814 processing of mineral dust: direct comparison of cloud residual and clear sky particles during
815 AMMA aircraft campaign in summer 2006, *Atmos. Chem. Phys.*, 10, 1057–1069,
816 <https://doi.org/10.5194/acp-10-1057-2010>, 2010.

817 Mayol-Bracero, O. L., Prospero, J. M., Sarangi, B., Andrews, E., Colarco, P. R., Cuevas, E., Di
818 Girolamo, L., Garcia, R. D., Gaston, C., Holben, B., Ladino, L. A., León, P., Losno, R.,
819 Martínez, O., Martínez-Huertas, B. L., Méndez-Lázaro, P., Molinie, J., Muller-Karger, F., Otis,
820 D., Raga, G., Reyes, A., Rosas Nava, J., Rosas, D., Sealy, A., Serikov, I., Tong, D., Torres-
821 Delgado, E., Yu, H., and Zuidema, P.: “Godzilla,” the Extreme African Dust Event of June 2020:
822 Origins, Transport, and Impact on Air Quality in the Greater Caribbean Basin, *Bull. Am.
823 Meteorol. Soc.*, 106, E1620–E1648, <https://doi.org/10.1175/BAMS-D-24-0045.1>, 2025.

824 Mehra, M., Shrestha, S., AP, K., Guagenti, M., Moffett, C. E., VerPloeg, S. G., Coogan, M. A.,
825 Rai, M., Kumar, R., Andrews, E., Sherman, J. P., Flynn III, J. H., Usenko, S., and Sheesley, R.
826 J.: Atmospheric heating in the US from saharan dust: Tracking the June 2020 event with surface
827 and satellite observations, *Atmos. Environ.*, 310, 119988,
828 <https://doi.org/10.1016/j.atmosenv.2023.119988>, 2023.

829 Meloni, D., di Sarra, A., Brogniez, G., Denjean, C., De Silvestri, L., Di Iorio, T., Formenti, P.,
830 Gómez-Amo, J. L., Gröbner, J., Kouremeti, N., Liuzzi, G., Mallet, M., Pace, G., and Sferlazzo,
831

832 D. M.: Determining the infrared radiative effects of Saharan dust: a radiative transfer modelling
833 study based on vertically resolved measurements at Lampedusa, *Atmos. Chem. Phys.*, 18, 4377–
834 4401, <https://doi.org/10.5194/acp-18-4377-2018>, 2018.

835 Moustaka, A., Kazadzis, S., Proestakis, E., Lopatin, A., Dubovik, O., Tourpali, K., Zerefos, C.,
836 Amiridis, V., and Gkikas, A.: Enhancing dust aerosols monitoring capabilities across North
837 Africa and the Middle East using the A-Train satellite constellation,
838 <https://doi.org/10.5194/egusphere-2025-888>, 24 March 2025.

839 Müller, D., Weinzierl, B., Petzold, A., Kandler, K., Ansmann, A., Müller, T., Tesche, M.,
840 Freudenthaler, V., Esselborn, M., Heese, B., Althausen, D., Schladitz, A., Otto, S., and
841 Knippertz, P.: Mineral dust observed with AERONET Sun photometer, Raman lidar, and in situ
842 instruments during SAMUM 2006: Shape-independent particle properties, *J. Geophys. Res.*
843 *Atmos.*, 115, <https://doi.org/10.1029/2009JD012520>, 2010.

844 Müller, D., Lee, K. -H., Gasteiger, J., Tesche, M., Weinzierl, B., Kandler, K., Müller, T.,
845 Toledano, C., Otto, S., Althausen, D., and Ansmann, A.: Comparison of optical and
846 microphysical properties of pure Saharan mineral dust observed with AERONET Sun
847 photometer, Raman lidar, and in situ instruments during SAMUM 2006, *J. Geophys. Res.*
848 *Atmos.*, 117, <https://doi.org/10.1029/2011JD016825>, 2012.

849 O'Dowd, C. D. and de Leeuw, G.: Marine aerosol production: a review of the current
850 knowledge, *Philos. Trans. R. Soc. A Math. Phys. Eng. Sci.*, 365, 1753–1774,
851 <https://doi.org/10.1098/rsta.2007.2043>, 2007.

852 O'Neill, N. T., Eck, T. F., Smirnov, A., Holben, B. N., and Thulasiraman, S.: Spectral
853 discrimination of coarse and fine mode optical depth, *J. Geophys. Res. Atmos.*, 108,
854 <https://doi.org/10.1029/2002JD002975>, 2003.

855 Orozco, D., Beyersdorf, A. J., Ziembba, L. D., Berkoff, T., Zhang, Q., Delgado, R., Hennigan, C.
856 J., Thornhill, K. L., Young, D. E., Parworth, C., Kim, H., and Hoff, R. M.: Hygroscopicity
857 measurements of aerosol particles in the San Joaquin Valley, CA, Baltimore, MD, and Golden,
858 CO, *J. Geophys. Res. Atmos.*, 121, 7344–7359, <https://doi.org/10.1002/2015JD023971>, 2016.

859 Proestakis, E., Amiridis, V., Marinou, E., Georgoulias, A. K., Solomos, S., Kazadzis, S., Chimot,
860 J., Che, H., Alexandri, G., Binietoglou, I., Daskalopoulou, V., Kourtidis, K. A., de Leeuw, G.,
861 and van der A, R. J.: Nine-year spatial and temporal evolution of desert dust aerosols over South
862 and East Asia as revealed by CALIOP, *Atmos. Chem. Phys.*, 18, 1337–1362,
863 <https://doi.org/10.5194/acp-18-1337-2018>, 2018.

864 Prospero, J. M.: Mineral and sea salt aerosol concentrations in various ocean regions, *J.*
865 *Geophys. Res. Ocean.*, 84, 725–731, <https://doi.org/10.1029/JC084iC02p00725>, 1979.

866 Prospero, J. M.: Long-term measurements of the transport of African mineral dust to the
867 southeastern United States: Implications for regional air quality, *J. Geophys. Res. Atmos.*, 104,
868 15917–15927, <https://doi.org/10.1029/1999JD900072>, 1999.

869 Prospero, J. M., Delany, A. C., Delany, A. C., and Carlson, T. N.: The Discovery of African Dust
870 Transport to the Western Hemisphere and the Saharan Air Layer: A History, *Bull. Am. Meteorol.*
871 *Soc.*, 102, E1239–E1260, <https://doi.org/10.1175/BAMS-D-19-0309.1>, 2021.

872 Razenkov, I.: Characterization of a Geiger-Mode Avalanche Photodiode Detector for High
873 Special Resolution Lidar, University of Wisconsin - Madison, 2010.

874 Reid, E. A., Reid, J. S., Meier, M. M., Dunlap, M. R., Cliff, S. S., Broumas, A., Perry, K., and
875 Maring, H.: Characterization of African dust transported to Puerto Rico by individual particle
876 and size segregated bulk analysis, *J. Geophys. Res. Atmos.*, 108,
877 <https://doi.org/10.1029/2002JD002935>, 2003a.

878 Reid, J. S., Jonsson, H. H., Maring, H. B., Smirnov, A., Savoie, D. L., Cliff, S. S., Reid, E. A.,
879 Livingston, J. M., Meier, M. M., Dubovik, O., and Tsay, S.: Comparison of size and
880 morphological measurements of coarse mode dust particles from Africa, *J. Geophys. Res.*
881 *Atmos.*, 108, <https://doi.org/10.1029/2002JD002485>, 2003b.

882 Reid, J. S., Holz, R. E., Hostetler, C. A., Ferrare, R. A., Rubin, J. I., Thompson, E. J., van den
883 Heever, S. C., Amiot, C. G., Burton, S. P., DiGangi, J. P., Diskin, G. S., Cossuth, J. H.,
884 Eleuterio, D. P., Eloranta, E. W., Kuehn, R., Marais, W. J., Maring, H. B., Sorooshian, A.,
885 Thornhill, K. L., Trepte, C. R., Wang, J., Xian, P., and Ziembba, L. D.: PISTON and CAMP 2 Ex
886 observations of the fundamental modes of aerosol vertical variability in the Northwest Tropical
887 Pacific and Maritime Continent's Monsoon, <https://doi.org/10.5194/egusphere-2025-2605>, 12
888 August 2025.

889 Riemer, N., Ault, A. P., West, M., Craig, R. L., and Curtis, J. H.: Aerosol Mixing State:
890 Measurements, Modeling, and Impacts, *Rev. Geophys.*, 57, 187–249,
891 <https://doi.org/10.1029/2018RG000615>, 2019.

892 Royer, H. M., Pöhlker, M. L., Krüger, O., Blades, E., Sealy, P., Lata, N. N., Cheng, Z., China, S.,
893 Ault, A. P., Quinn, P. K., Zuidema, P., Pöhlker, C., Pöschl, U., Andreae, M., and Gaston, C. J.:
894 African smoke particles act as cloud condensation nuclei in the wintertime tropical North
895 Atlantic boundary layer over Barbados, *Atmos. Chem. Phys.*, 23, 981–998,
896 <https://doi.org/10.5194/acp-23-981-2023>, 2023.

897 Royer, H. M., Sheridan, M. T., Elliott, H. E., Lata, N. N., Cheng, Z., China, S., Zhu, Z., Ault, A.
898 P., and Gaston, C. J.: African dust transported to Barbados in the Wintertime Lacks Indicators of
899 Chemical Aging, *Atmos. Chem. Phys.*, <https://doi.org/10.5194/egusphere-2024-3288>, 2025.

900 Scheuvens, D., Schütz, L., Kandler, K., Ebert, M., and Weinbruch, S.: Bulk composition of
901 northern African dust and its source sediments — A compilation, *Earth-Science Rev.*, 116, 170–
902 194, <https://doi.org/10.1016/j.earscirev.2012.08.005>, 2013.

903 Shen, H., Peters, T. M., Casuccio, G. S., Lersch, T. L., West, R. R., Kumar, A., Kumar, N., and
904 Ault, A. P.: Elevated Concentrations of Lead in Particulate Matter on the Neighborhood-Scale in
905 Delhi, India As Determined by Single Particle Analysis, *Environ. Sci. Technol.*, 50, 4961–4970,
906 <https://doi.org/10.1021/acs.est.5b06202>, 2016.

907 Stevens, B., Farrell, D., Hirsch, L., Jansen, F., Nuijens, L., Serikov, I., Brügmann, B., Forde, M.,
908 Linne, H., Lonitz, K., and Prospero, J. M.: The Barbados Cloud Observatory: Anchoring
909 Investigations of Clouds and Circulation on the Edge of the ITCZ, *Bull. Am. Meteorol. Soc.*, 97,
910 787–801, <https://doi.org/https://doi.org/10.1175/BAMS-D-14-00247.1>, 2016.

911 Tesche, M., Müller, D., Gross, S., Ansmann, A., Althausen, D., Freudenthaler, V., Weinzierl, B.,
912 Veira, A., and Petzold, A.: Optical and microphysical properties of smoke over Cape Verde
913 inferred from multiwavelength lidar measurements, *Tellus B Chem. Phys. Meteorol.*, 63, 677,
914 <https://doi.org/10.1111/j.1600-0889.2011.00549.x>, 2011.

915 Titos, G., Cazorla, A., Zieger, P., Andrews, E., Lyamani, H., Granados-Muñoz, M. J., Olmo, F.

916 J., and Alados-Arboledas, L.: Effect of hygroscopic growth on the aerosol light-scattering
917 coefficient: A review of measurements, techniques and error sources, *Atmos. Environ.*, 141,
918 494–507, <https://doi.org/10.1016/j.atmosenv.2016.07.021>, 2016.

919 Tsamalis, C., Chédin, A., Pelon, J., and Capelle, V.: The seasonal vertical distribution of the
920 Saharan Air Layer and its modulation by the wind, *Atmos. Chem. Phys.*, 13, 11235–11257,
921 <https://doi.org/10.5194/acp-13-11235-2013>, 2013.

922 Weinzierl, B., Ansmann, A., Prospero, J. M., Althausen, D., Benker, N., Chouza, F., Dollner, M.,
923 Farrell, D., Fomba, W. K., Freudenthaler, V., Gasteiger, J., Groß, S., Haarig, M., Heinold, B.,
924 Kandler, K., Kristensen, T. B., Mayol-Bracero, O. L., Müller, T., Reitebuch, O., Sauer, D.,
925 Schäfler, A., Schepanski, K., Spanu, A., Tegen, I., Toledano, C., and Walser, A.: The Saharan
926 Aerosol Long-Range Transport and Aerosol–Cloud-Interaction Experiment: Overview and
927 Selected Highlights, *Bull. Am. Meteorol. Soc.*, 98, 1427–1451, <https://doi.org/10.1175/BAMS-D-15-00142.1>, 2017.

928 Winkler, P.: The growth of atmospheric aerosol particles as a function of the relative humidity—
929 II. An improved concept of mixed nuclei, *J. Aerosol Sci.*, 4, 373–387,
930 [https://doi.org/10.1016/0021-8502\(73\)90027-X](https://doi.org/10.1016/0021-8502(73)90027-X), 1973.

931 World Health Organization: WHO global air quality guidelines. Particulate matter (PM_{2.5} and
932 PM₁₀), ozone, nitrogen dioxide, sulfur dioxide and carbon monoxide, Geneva, 290 pp., 2021.

933 Xian, P., Reid, J. S., Hyer, E. J., Sampson, C. R., Rubin, J. I., Ades, M., Asencio, N., Basart, S.,
934 Benedetti, A., Bhattacharjee, P. S., Brooks, M. E., Colarco, P. R., da Silva, A. M., Eck, T. F.,
935 Guth, J., Jorba, O., Kouznetsov, R., Kipling, Z., Sofiev, M., Perez Garcia-Pando, C., Pradhan,
936 Y., Tanaka, T., Wang, J., Westphal, D. L., Yumimoto, K., and Zhang, J.: Current state of the
937 global operational aerosol multi-model ensemble: An update from the International Cooperative
938 for Aerosol Prediction (ICAP), *Q. J. R. Meteorol. Soc.*, 145, 176–209,
939 <https://doi.org/10.1002/qj.3497>, 2019.

940 Yang, L., Zhang, S., Tao, H., Yang, Y., Wang, L., Cui, Y., Xu, Y., and Li, X.: Comprehensive
941 Analysis of a Dust Storm by a Lidar Network Combined With Multiple Data, *Front. Environ.*
942 *Sci.*, 10, <https://doi.org/10.3389/fenvs.2022.832710>, 2022.

943 Yang, W., Marshak, A., Várnai, T., Kalashnikova, O. V., and Kostinski, A. B.: CALIPSO
944 observations of transatlantic dust: vertical stratification and effect of clouds, *Atmos. Chem.*
945 *Phys.*, 12, 11339–11354, <https://doi.org/10.5194/acp-12-11339-2012>, 2012.

946 Zhang, D. and Iwasaka, Y.: Chlorine deposition on dust particles in marine atmosphere,
947 *Geophys. Res. Lett.*, 28, 3613–3616, <https://doi.org/10.1029/2001GL013333>, 2001.

948 Zhang, D. and Iwasaka, Y.: Size change of Asian dust particles caused by sea salt interaction:
949 Measurements in southwestern Japan, *Geophys. Res. Lett.*, 31,
950 <https://doi.org/10.1029/2004GL020087>, 2004.

951 Zhang, D., Zang, J., Shi, G., Iwasaka, Y., Matsuki, A., and Trochkine, D.: Mixture state of
952 individual Asian dust particles at a coastal site of Qingdao, China, *Atmos. Environ.*, 37, 3895–
953 3901, [https://doi.org/10.1016/S1352-2310\(03\)00506-5](https://doi.org/10.1016/S1352-2310(03)00506-5), 2003.

954 Zhang, D., Iwasaka, Y., Matsuki, A., Ueno, K., and Matsuzaki, T.: Coarse and accumulation
955 mode particles associated with Asian dust in southwestern Japan, *Atmos. Environ.*, 40, 1205–
956 1215, <https://doi.org/10.1016/j.atmosenv.2005.10.037>, 2006.

957

958 Zhang, X., Massoli, P., Quinn, P. K., Bates, T. S., and Cappa, C. D.: Hygroscopic growth of
959 submicron and supermicron aerosols in the marine boundary layer, *J. Geophys. Res. Atmos.*,
960 119, 8384–8399, <https://doi.org/10.1002/2013JD021213>, 2014.

961 Zieger, P., Väisänen, O., Corbin, J. C., Partridge, D. G., Bastelberger, S., Mousavi-Fard, M.,
962 Rosati, B., Gysel, M., Krieger, U. K., Leck, C., Nenes, A., Riipinen, I., Virtanen, A., and Salter,
963 M. E.: Revising the hygroscopicity of inorganic sea salt particles, *Nat. Commun.*, 8,
964 <https://doi.org/10.1038/ncomms15883>, 2017.

965 Zuidema, P., Alvarez, C., Kramer, S. J., Custals, L., Izaguirre, M., Sealy, P., Prospero, J. M., and
966 Blades, E.: Is Summer African Dust Arriving Earlier to Barbados? The Updated Long-Term In
967 Situ Dust Mass Concentration Time Series from Ragged Point, Barbados, and Miami, Florida,
968 *Bull. Am. Meteorol. Soc.*, 100, 1981–1986, <https://doi.org/10.1175/BAMS-D-18-0083.1>, 2019.

969